2012

Excited-state spectroscopy of triply bottom baryons from lattice QCD

Stefan Meinel
William & Mary

Recommended Citation

Meinel, Stefan, Excited-state spectroscopy of triply bottom baryons from lattice QCD (2012). *Physical Review D*, 85(11).
10.1103/PhysRevD.85.114510

PHYSICAL REVIEW D **85,** 114510 (2012)

Excited-state spectroscopy of triply bottom baryons from lattice QCD

Stefan Meinel

Department of Physics, College of William & Mary, Williamsburg, Virginia 23187-8795, USA

(Received 14 February 2012; published 25 June 2012)

The spectrum of baryons containing three b quarks is calculated in nonperturbative QCD, using the lattice regularization. The energies of ten excited bbb states with $J^P = \frac{1}{2}^+, \frac{3}{2}^+, \frac{5}{2}^+, \frac{7}{2}^+, \frac{1}{2}^-$, and $\frac{3}{2}^-$ are determined with high precision. A domain-wall action is used for the up, down, and strange quarks, and the bottom quarks are implemented with nonrelativistic QCD. The computations are done at lattice spacings of $a \approx 0.11$ fm and $a \approx 0.08$ fm, and the results demonstrate the improvement of rotational symmetry as a is reduced. A large lattice volume of $(2.7\text{ fm})^3$ is used, and extrapolations of the bbb spectrum to realistic values of the light sea-quark masses are performed. All spin-dependent energy splittings are resolved with total uncertainties of order 1 MeV, and the dependence of these splittings on the couplings in the nonrelativistic QCD action is analyzed.

DOI: 10.1103/PhysRevD.85.114510 PACS numbers: 12.38.Gc, 14.20.Mr

I. INTRODUCTION

Heavy quarkonium has been studied in great detail both experimentally and theoretically. Because its valence quark masses are large compared to Λ_{QCD}, heavy quarkonium is an excellent system for probing the strong force on multiple scales [1]. In addition to these familiar heavy quark-antiquark bound states, QCD also predicts the existence of an analogous system in the baryonic sector: the bound states of three heavy quarks. Given the huge importance of quarkonium, it is desirable to investigate triply heavy baryons in similar depth.

Several continuum-based calculations of triply heavy baryon spectra can be found in the literature. The methods used there include quark models [2–17], QCD sum rules [18,19], and potential nonrelativistic QCD (pNRQCD) with static potentials from perturbation theory, at leading order [20], and next-to-next-to-leading order [21,22]. No experimental results are available so far for triply heavy baryons (see Ref. [23] for a recent calculation of production cross sections at the LHC). This means that first-principles nonperturbative lattice QCD calculations are essential to test the model-dependent or perturbative approaches. For the Ω_{bbb}, the ground-state mass was already calculated with high precision using lattice QCD in Ref. [24]. However, much more information about the interactions between three heavy quarks can be gained by computing the spectrum of the corresponding excited states, including, in particular, the spin-dependent energy splittings. The first such calculation of bbb excited states in lattice QCD is reported here. Lattice calculations of light-baryon excited states can be found, for example, in Refs. [25–33].

To fully accommodate the physics of the light sea quarks in lattice QCD, the spatial box size L has to be chosen such that $L \gg 1/m_\pi$. With the presently available computing resources, this requirement means that the lattice spacing is too coarse to treat the b quarks in the same way as the light quarks. Therefore, as in Ref. [24], the b quarks are implemented here with improved lattice nonrelativistic QCD (NRQCD) [34,35]. NRQCD is an effective field theory for heavy quarks that retains all the gluon and light-quark degrees of freedom without change. For the heavy-quark Lagrangian, a nonrelativistic expansion is performed in powers of the heavy-quark velocity v, and the coefficients of the NRQCD effective operators are determined by matching to QCD. Thereby, the results of QCD can be reproduced, in principle, to an arbitrary order in v. For $b\bar{b}$ and bbb hadrons, one has $\langle v^2 \rangle \approx 0.1$. The lattice NRQCD action used in Ref. [24] was complete through order v^4. Because the present work aims to accurately compute also spin-dependent bbb energy splittings (fine and hyperfine structure), here the spin-dependent order-v^6 terms are included in the NRQCD action, as already done in the calculation of the bottomonium spectrum of Ref. [36]. Furthermore, the coefficients of the leading spin-dependent operators, which are of order v^4, are tuned nonperturbatively.

As usual in lattice QCD, the Euclidean path integral is performed by averaging over importance-sampled gauge-field configurations. The ensembles of gauge fields used here match those used in Refs. [24,36], and have been generated by the RBC/UKQCD Collaboration [37]. These ensembles include the effects of dynamical u, d, and s quarks, which were implemented using a domain-wall action [38–40]. Seven different ensembles with a range of light-quark masses and lattice spacings of $a \approx 0.11$ fm and $a \approx 0.08$ fm are included in the analysis.

The bbb energy levels are extracted from the time dependence of Euclidean two-point functions of interpolating operators with the desired quantum numbers. The construction of these interpolating operators, which takes into account the reduction of the continuum rotational symmetries to the lattice rotational symmetries, follows the highly successful method originally developed for light baryons in Ref. [33]. This method, as well as the computation of the bbb two-point functions, is explained in Sec. II. The details of the lattice actions and parameters

are given in Sec. III. Next, Sec. IV describes the fitting of the two-point functions and the angular momentum identification. The spectrum results are extrapolated in the light-quark masses to obtain the final results in Sec. V. An additional section (Sec. VI) is devoted to investigating the dependence of the bbb energy splittings on the various operators in the NRQCD action.

II. CONSTRUCTION OF BARYON INTERPOLATING OPERATORS

In this section we construct interpolating operators, Ω, that give access to bbb states up to $J = \frac{7}{2}$. The method is taken from Ref. [33], but is described again in the following specifically for the case needed here, where all three quark flavors are equal and only two-component Pauli spinors are used. Going through the derivation of the interpolating operators also gives some insight into the structure of the bbb states extracted in the numerical part of the calculation. However, it is important to remember that the spectrum calculated here is that of the (lattice) QCD + NRQCD Hamiltonian: $H_{\mathrm{QCD}}|n\rangle = E_n|n\rangle$. The interpolating operators determine only the overlap factors $\langle n|\Omega|0\rangle$, not the energies E_n. For the numerical calculation it is nevertheless advantageous to construct operators that have large overlaps only with selected bbb states, to get good statistical precision for the energy levels and identify their angular momentum J.

A key feature of the approach from Ref. [33] is the initial construction of operators with definite quantum numbers J and m according to the *continuum* rotational symmetry (Sec. II A). This is then followed by the *subduction*, where linear combinations of the different m components at a given J are formed such that these transform irreducibly under the lattice rotational symmetries (Sec. II B). The numerical calculations demonstrate that the rotational symmetry breaking is very weak, and operators subduced from continuum operators with different values of J retain an approximate orthogonality even if they fall in the same irreducible representation of the octahedral group. This feature dramatically simplifies the angular momentum identification for the extracted energy levels.

Following the group-theoretical operator construction, Sec. II C then describes the initial smearing of the quark fields and the calculation of the baryon two-point functions on the lattice.

A. Operators with definite continuum J

In all baryon operators, the colors of the three quarks are combined into a singlet using the totally antisymmetric color wave function ϵ_{abc}. In the case considered here, the three quarks have equal flavor. Therefore, to satisfy the Pauli principle, the product of the spin and spatial wave functions must be totally symmetric. The spatial structure is obtained by applying up to two derivative operators to Gaussian-smeared quark fields. The derivatives are combined to a definite total orbital angular momentum L and a definite permutation symmetry. Similarly, the spins of the three quarks are combined to a definite total spin S and definite permutation symmetry. Finally, the derivative and spin wave functions obtained in these two separate steps are combined to obtain baryon operators with a definite total angular momentum J and the desired total symmetry of the product of the spin and spatial wave functions. Note that L and S are not conserved quantum numbers and are only used to label the structure of the interpolating operators.

We begin by combining the three quark fields to definite total spin S. Because NRQCD is used for the heavy quarks, there are only two spin components, denoted by $\tilde{\psi}_\uparrow$ and $\tilde{\psi}_\downarrow$. The color indices are omitted here, but remain uncontracted at this stage (the contraction with ϵ_{abc} is only performed after the gauge-covariant derivatives have been applied). The $S = \frac{3}{2}$ combinations are given by

$$\begin{aligned}
O_{\mathsf{S}}(\tfrac{3}{2}, +\tfrac{3}{2}) &= \tilde{\psi}_\uparrow\tilde{\psi}_\uparrow\tilde{\psi}_\uparrow,\\
O_{\mathsf{S}}(\tfrac{3}{2}, +\tfrac{1}{2}) &= \frac{1}{\sqrt{3}}(\tilde{\psi}_\uparrow\tilde{\psi}_\uparrow\tilde{\psi}_\downarrow + \tilde{\psi}_\uparrow\tilde{\psi}_\downarrow\tilde{\psi}_\uparrow + \tilde{\psi}_\downarrow\tilde{\psi}_\uparrow\tilde{\psi}_\uparrow),\\
O_{\mathsf{S}}(\tfrac{3}{2}, -\tfrac{1}{2}) &= \frac{1}{\sqrt{3}}(\tilde{\psi}_\downarrow\tilde{\psi}_\downarrow\tilde{\psi}_\uparrow + \tilde{\psi}_\downarrow\tilde{\psi}_\uparrow\tilde{\psi}_\downarrow + \tilde{\psi}_\uparrow\tilde{\psi}_\downarrow\tilde{\psi}_\downarrow),\\
O_{\mathsf{S}}(\tfrac{3}{2}, -\tfrac{3}{2}) &= \tilde{\psi}_\downarrow\tilde{\psi}_\downarrow\tilde{\psi}_\downarrow,
\end{aligned} \tag{1}$$

where the subscript S indicates the total symmetry under permutations. For $S = \frac{1}{2}$, one can construct both mixed-symmetric (MS) and mixed-antisymmetric (MA) combinations:

$$\begin{aligned}
O_{\mathsf{MS}}(\tfrac{1}{2}, +\tfrac{1}{2}) &= \frac{1}{\sqrt{6}}(\tilde{\psi}_\uparrow\tilde{\psi}_\downarrow\tilde{\psi}_\uparrow + \tilde{\psi}_\downarrow\tilde{\psi}_\uparrow\tilde{\psi}_\uparrow - 2\tilde{\psi}_\uparrow\tilde{\psi}_\uparrow\tilde{\psi}_\downarrow),\\
O_{\mathsf{MS}}(\tfrac{1}{2}, -\tfrac{1}{2}) &= -\frac{1}{\sqrt{6}}(\tilde{\psi}_\downarrow\tilde{\psi}_\uparrow\tilde{\psi}_\downarrow + \tilde{\psi}_\uparrow\tilde{\psi}_\downarrow\tilde{\psi}_\downarrow - 2\tilde{\psi}_\downarrow\tilde{\psi}_\downarrow\tilde{\psi}_\uparrow),
\end{aligned} \tag{2}$$

$$\begin{aligned}
O_{\mathsf{MA}}(\tfrac{1}{2}, +\tfrac{1}{2}) &= \frac{1}{\sqrt{2}}(\tilde{\psi}_\uparrow\tilde{\psi}_\downarrow\tilde{\psi}_\uparrow - \tilde{\psi}_\downarrow\tilde{\psi}_\uparrow\tilde{\psi}_\uparrow),\\
O_{\mathsf{MA}}(\tfrac{1}{2}, -\tfrac{1}{2}) &= -\frac{1}{\sqrt{2}}(\tilde{\psi}_\downarrow\tilde{\psi}_\uparrow\tilde{\psi}_\downarrow - \tilde{\psi}_\uparrow\tilde{\psi}_\downarrow\tilde{\psi}_\downarrow).
\end{aligned} \tag{3}$$

Next, we come to the derivatives. A single derivative is an $L = 1$ object, with m components given by

$$D_{\pm1} = \pm\frac{i}{2}(D_x \pm iD_y), \qquad D_0 = -\frac{i}{\sqrt{2}}D_z. \tag{4}$$

Recall that in this section we work in continuous space; lattice derivatives will be defined in Sec. II C. In the following, we use the notation $D_m^{(k)}$ for a derivative acting on the kth quark in the baryon operator. As in Ref. [33], we define the following combinations with definite permutation symmetry:

$$D^{[1]}_{\mathsf{MS}}(1,m) = \frac{1}{\sqrt{6}}(2D^{(3)}_m - D^{(1)}_m - D^{(2)}_m),$$
$$D^{[1]}_{\mathsf{MA}}(1,m) = \frac{1}{\sqrt{2}}(D^{(1)}_m - D^{(2)}_m). \tag{5}$$

(No totally antisymmetric combination exists, and the totally symmetric combination vanishes at zero momentum.) Using the Clebsch-Gordan coefficients $\langle L, m|1, m_1; 1, m_2\rangle$, we can combine two single-derivative operators of the form (5) into double-derivative operators with definite total L and definite permutation symmetry as follows [33]:

$$\begin{aligned}
D^{[2]}_{\mathsf{S}}(L,m) &= \frac{1}{\sqrt{2}}\sum_{m_1,m_2}\langle L,m|1,m_1;1,m_2\rangle(+D^{[1]}_{\mathsf{MS}}(1,m_1)D^{[1]}_{\mathsf{MS}}(1,m_2) + D^{[1]}_{\mathsf{MA}}(1,m_1)D^{[1]}_{\mathsf{MA}}(1,m_2)),\\
D^{[2]}_{\mathsf{MS}}(L,m) &= \frac{1}{\sqrt{2}}\sum_{m_1,m_2}\langle L,m|1,m_1;1,m_2\rangle(-D^{[1]}_{\mathsf{MS}}(1,m_1)D^{[1]}_{\mathsf{MS}}(1,m_2) + D^{[1]}_{\mathsf{MA}}(1,m_1)D^{[1]}_{\mathsf{MA}}(1,m_2)),\\
D^{[2]}_{\mathsf{MA}}(L,m) &= \frac{1}{\sqrt{2}}\sum_{m_1,m_2}\langle L,m|1,m_1;1,m_2\rangle(+D^{[1]}_{\mathsf{MS}}(1,m_1)D^{[1]}_{\mathsf{MA}}(1,m_2) + D^{[1]}_{\mathsf{MA}}(1,m_1)D^{[1]}_{\mathsf{MS}}(1,m_2)),\\
D^{[2]}_{\mathsf{A}}(1,m) &= \frac{1}{\sqrt{2}}\sum_{m_1,m_2}\langle 1,m|1,m_1;1,m_2\rangle(+D^{[1]}_{\mathsf{MS}}(1,m_1)D^{[1]}_{\mathsf{MA}}(1,m_2) - D^{[1]}_{\mathsf{MA}}(1,m_1)D^{[1]}_{\mathsf{MS}}(1,m_2)).
\end{aligned} \tag{6}$$

The first three of the above combinations can give either $L = 0$ or $L = 2$, while the last combination is restricted to $L = 1$.

Now we can combine the spin and spatial wave functions, distinguishing the cases of zero, one, and two derivatives. Without derivatives, the requirement of total symmetry restricts the spin to $S = \frac{3}{2}$. Since $L = 0$, we only get $J = \frac{3}{2}$ in this case:

$$[O_{\mathsf{S}}(\tfrac{3}{2})]^{J=3/2}_m = O_{\mathsf{S}}(\tfrac{3}{2}, m). \tag{7}$$

In one-derivative baryon operators, the derivative part, Eq. (5), always has mixed symmetry. Therefore, to get a totally symmetric combination, the spin part must also have mixed symmetry, and hence $S = \frac{1}{2}$. Because the derivative has $L = 1$, we can combine L and S to the total angular momenta $J = \frac{1}{2}$ and $J = \frac{3}{2}$:

$$[D^{[1]}_{\mathsf{M}}(1)O_{\mathsf{M}}(\tfrac{1}{2})]^{J=1/2,3/2}_m = \frac{1}{\sqrt{2}}\sum_{m_1,m_2}\langle J,m|1,m_1;\tfrac{1}{2},m_2\rangle(D^{[1]}_{\mathsf{MS}}(1,m_1)O_{\mathsf{MS}}(\tfrac{1}{2},m_2) + D^{[1]}_{\mathsf{MA}}(1,m_1)O_{\mathsf{MA}}(\tfrac{1}{2},m_2)). \tag{8}$$

Finally, we consider the double-derivative operators. Because no totally antisymmetric spin combinations exist, the totally antisymmetric derivative combination in the last line of Eq. (6) is excluded, and the two derivatives can only combine to $L = 0$ or $L = 2$. In each case, one can have $S = \frac{1}{2}$ with mixed symmetry or $S = \frac{3}{2}$ with total symmetry. Thus, one obtains the following combinations:

$$\begin{aligned}
[D^{[2]}_{\mathsf{S}}(0)O_{\mathsf{S}}(\tfrac{3}{2})]^{J=3/2}_m &= D^{[2]}_{\mathsf{S}}(0,0)O_{\mathsf{S}}(\tfrac{3}{2},m),\\
[D^{[2]}_{\mathsf{M}}(0)O_{\mathsf{M}}(\tfrac{1}{2})]^{J=1/2}_m &= \frac{1}{\sqrt{2}}(D^{[2]}_{\mathsf{MS}}(0,0)O_{\mathsf{MS}}(\tfrac{1}{2},m) + D^{[2]}_{\mathsf{MA}}(0,0)O_{\mathsf{MA}}(\tfrac{1}{2},m)),\\
[D^{[2]}_{\mathsf{M}}(2)O_{\mathsf{M}}(\tfrac{1}{2})]^{J=3/2,5/2}_m &= \frac{1}{\sqrt{2}}\sum_{m_1,m_2}\langle J,m|2,m_1;\tfrac{1}{2},m_2\rangle(D^{[2]}_{\mathsf{MS}}(2,m_1)O_{\mathsf{MS}}(\tfrac{1}{2},m_2) + D^{[2]}_{\mathsf{MA}}(2,m_1)O_{\mathsf{MA}}(\tfrac{1}{2},m)),\\
[D^{[2]}_{\mathsf{S}}(2)O_{\mathsf{S}}(\tfrac{3}{2})]^{J=1/2,3/2,5/2,7/2}_m &= \sum_{m_1,m_2}\langle J,m|2,m_1;\tfrac{3}{2},m_2\rangle D^{[2]}_{\mathsf{S}}(2,m_1)O_{\mathsf{S}}(\tfrac{3}{2},m_2).
\end{aligned} \tag{9}$$

Note that the combination with $D^{[2]}_{\mathsf{S}}(0,0)$, which corresponds to the spatial Laplacian, was excluded in Ref. [33] with the argument that it vanishes at zero momentum. However, this is not the case for the method of smearing the quark fields and constructing the two-point functions described in Sec. II C. In fact, the operator $[D^{[2]}_{\mathsf{S}}(0)O_{\mathsf{S}}(\frac{3}{2})]^{J=3/2}_m$ has a good overlap with the first radially excited $J = \frac{3}{2}$ state, and including this operator in the basis significantly improves the extraction of this energy level.

B. Subduction to irreducible representations of the double cover of the octahedral group

In the previous section, we constructed operators $[\Omega]^J_m$ that transform under rotations like the basis vectors $|J, m\rangle$ of irreducible representations of $SU(2)$. The group $SU(2)$ is the double cover of the continuum three-dimensional rotation group $SO(3)$. On a cubic lattice, the rotational symmetry is reduced to the discrete group ^{2}O, the double cover of the octahedral group O. The group ^{2}O, which is obtained from O by adding a negative identity for $\pm 2\pi$ rotations, has 48 elements in eight conjugacy classes. Correspondingly, ^{2}O has eight irreducible representations denoted as A_1, A_2, E, T_1, T_2, G_1, G_2, H (see, for example, Ref. [41]). Their dimensions are 1, 1, 2, 3, 3, 2, 2, 4, respectively. Starting from an operator $[\Omega]^J_m$, it is possible to form suitable linear combinations of its different m components, so that these linear combinations transform in irreducible representations, Λ, of the double-cover octahedral group:

$$[\Omega]^J_{{}^n\Lambda,r} = \sum_m \mathcal{S}^{J,m}_{{}^n\Lambda,r}[\Omega]^J_m. \tag{10}$$

This process is referred to as reduction or subduction [33,41], and the coefficients $\mathcal{S}^{J,m}_{{}^n\Lambda,r}$ form the subduction matrices. Here, ${}^n\Lambda$ denotes the nth occurrence of an irrep Λ of ^{2}O, and $r = 1, \ldots, \dim(\Lambda)$ denotes its row [like m denotes the row for the $SU(2)$ irrep]. For each value of J, only selected irreps of ^{2}O appear in the subduction, such that the sum of their dimensions equals $2J + 1$ [the dimension of the original $SU(2)$ irrep J]. This is indicated in Table I. For integer values of J, only the irreps A_1, A_2, E, T_1, and T_2 appear. Conversely, for half-integer J, only the irreps G_1, G_2, and H occur. Since we are considering baryons, we will only be concerned with these three irreps in the remainder of the paper. The subduction matrices for $(J = \frac{1}{2}) \to G_1$ and $(J = \frac{3}{2}) \to H$ are simply the 2×2 and 4×4 identity matrices, so that, for example, $[\Omega]^{1/2}_{G_1,1} = [\Omega]^{1/2}_{+1/2}$ and $[\Omega]^{1/2}_{G_1,2} = [\Omega]^{1/2}_{-1/2}$. The subduction matrices for $J = \frac{5}{2}$ and $J = \frac{7}{2}$ can be found in Ref. [33].

So far we have only discussed the rotational symmetry. Additionally, we can classify the operators according to their transformation properties under space inversion, which remains an exact symmetry on the lattice. Then all of the irreducible representations come in parity-even and parity-odd versions, as indicated by subscripts g (gerade) and u (ungerade): $A_{1g}, \ldots, T_{2g}$, G_{1g}, G_{2g}, H_g, and $A_{1u}, \ldots, T_{2u}$, G_{1u}, G_{2u}, H_u. In this work, the baryon operators are constructed from two-component NRQCD spinors, and therefore the parity of an operator is determined entirely by the number of derivatives it contains: an even number of derivatives corresponds to even parity and an odd number of derivatives corresponds to odd parity.

The 11 different baryon operators constructed in Eqs. (7)–(9) subduce to seven operators in the H_g irrep, three operators each in the G_{1g} and G_{2g} irreps, and one operator each in the G_{1u} and H_u irreps. This set of operators is summarized in Table II.

TABLE I. Subduction of $SU(2)$ irreps to ^{2}O irreps, up to $J = \frac{9}{2}$ (from Ref. [41]).

J	Subduction
0	A_1
1/2	G_1
1	T_1
3/2	H
2	$E + T_2$
5/2	$G_2 + H$
3	$A_2 + T_1 + T_2$
7/2	$G_1 + G_2 + H$
4	$A_1 + E + T_1 + T_2$
9/2	$G_1 + {}^1H + {}^2H$

C. Computation of two-point functions on the lattice

The group-theoretical construction of baryon operators through subduction was performed here in the same way as done for light baryons in Ref. [33]. However, the method for smearing the quark fields and computing the two-point functions in terms of quark propagators differs from that used in Ref. [33]. Instead of *distillation* [42], here the more traditional approach starting from Gaussian-smeared point sources, as in Ref. [43], is chosen. This has the advantage over distillation that the quark smearing width can be made very narrow without increasing the computational cost. A narrow smearing width is needed to get a good overlap with the physical bbb states, which are expected to be very small objects as a consequence of the large b-quark mass.

In the approach used here, the smeared b-quark fields $\tilde{\psi}$ entering in Eqs. (1)–(3) are defined in terms of the unsmeared quark fields ψ through

TABLE II. Interpolating operators, named according to their parity (g: +; u: −) and irreducible representation of ^{2}O. The superscript labels the different operators within a given irrep and parity.

Operator(s)	Structure $\sim[D(L)O(S)]^J$
$H_g^{(1)}$	$[O_{\mathsf{S}}(\frac{3}{2})]^{J=3/2}$
$G_{1u}^{(1)}$	$[D^{[1]}_{\mathsf{M}}(1)O_{\mathsf{M}}(\frac{1}{2})]^{J=1/2}$
$H_u^{(1)}$	$[D^{[1]}_{\mathsf{M}}(1)O_{\mathsf{M}}(\frac{1}{2})]^{J=3/2}$
$H_g^{(2)}$	$[D^{[2]}_{\mathsf{S}}(0)O_{\mathsf{S}}(\frac{3}{2})]^{J=3/2}$
$G_{1g}^{(1)}$	$[D^{[2]}_{\mathsf{M}}(0)O_{\mathsf{M}}(\frac{1}{2})]^{J=1/2}$
$G_{1g}^{(2)}$	$[D^{[2]}_{\mathsf{S}}(2)O_{\mathsf{S}}(\frac{3}{2})]^{J=1/2}$
$H_g^{(3)}$	$[D^{[2]}_{\mathsf{S}}(2)O_{\mathsf{S}}(\frac{3}{2})]^{J=3/2}$
$H_g^{(4)}$, $G_{2g}^{(1)}$	$[D^{[2]}_{\mathsf{S}}(2)O_{\mathsf{S}}(\frac{3}{2})]^{J=5/2}$
$H_g^{(5)}$, $G_{1g}^{(3)}$, $G_{2g}^{(2)}$	$[D^{[2]}_{\mathsf{S}}(2)O_{\mathsf{S}}(\frac{3}{2})]^{J=7/2}$
$H_g^{(6)}$	$[D^{[2]}_{\mathsf{M}}(2)O_{\mathsf{M}}(\frac{1}{2})]^{J=3/2}$
$H_g^{(7)}$, $G_{2g}^{(3)}$	$[D^{[2]}_{\mathsf{M}}(2)O_{\mathsf{M}}(\frac{1}{2})]^{J=5/2}$

$$\tilde{\psi} = \left(1 + \frac{r_S^2}{2n_S}\Delta^{(2)}\right)^{n_S}\psi, \tag{11}$$

where $\Delta^{(2)}$ is a three-dimensional gauge-covariant lattice Laplace operator,

$$\Delta^{(2)}\psi(\boldsymbol{x}, t) = -\frac{1}{a^2}\sum_{j=1}^{3}(\tilde{U}_j(\boldsymbol{x}, t)\psi(\boldsymbol{x} + a\hat{\boldsymbol{j}}, t) - 2\psi(\boldsymbol{x}, t) + \tilde{U}_{-j}(\boldsymbol{x}, t)\psi(\boldsymbol{x} - a\hat{\boldsymbol{j}}, t)). \tag{12}$$

In this work, a smearing radius of $r_S \approx 0.14$ fm is used in Eq. (11). The gauge-covariant derivatives in the baryon operators then act on these smeared quark fields. The continuous derivatives D_j used in Sec. II A are replaced by lattice versions ∇_j, which are defined as

$$\nabla_j\tilde{\psi}(\boldsymbol{x}, t) = \frac{1}{2a}(\tilde{U}_j(\boldsymbol{x}, t)\tilde{\psi}(\boldsymbol{x} + a\hat{\boldsymbol{j}}, t) - \tilde{U}_{-j}(\boldsymbol{x}, t)\tilde{\psi}(\boldsymbol{x} - a\hat{\boldsymbol{j}}, t)). \tag{13}$$

The tilde on the gauge links in Eqs. (12) and (13) indicates that these are also smeared, using the procedure of Ref. [44]. The gauge link smearing in the hadron interpolating fields is performed to reduce statistical noise [43]. The baryon operators constructed in the previous two sections contain quark fields with up to two derivatives. It is convenient to introduce new objects $\tilde{\psi}_i$, where i labels all the required 13 derivative combinations:

$$\begin{aligned}
\tilde{\psi}_1 &= \tilde{\psi},\\
\tilde{\psi}_2 &= \nabla_x\tilde{\psi},\\
\tilde{\psi}_3 &= \nabla_y\tilde{\psi},\\
\tilde{\psi}_4 &= \nabla_z\tilde{\psi},\\
\tilde{\psi}_5 &= \nabla_x\nabla_x\tilde{\psi},\\
\tilde{\psi}_6 &= \nabla_y\nabla_x\tilde{\psi},\\
&\vdots\\
\tilde{\psi}_{13} &= \nabla_z\nabla_z\tilde{\psi}.
\end{aligned} \tag{14}$$

In addition to the derivative index $i = 1, \ldots, 13$, these fields $\tilde{\psi}_i = (\tilde{\psi}_{a\alpha i})$ have a color index $a = 1, 2, 3$ and a spinor index $\alpha = 1, 2$ ($=\uparrow, \downarrow$). Then, all baryon interpolating operators used here have the form

$$\Omega_\Gamma(\boldsymbol{x}, t) = \Gamma_{\alpha i\beta j\gamma k}\epsilon_{abc}\tilde{\psi}_{a\alpha i}(\boldsymbol{x}, t)\tilde{\psi}_{b\beta j}(\boldsymbol{x}, t)\tilde{\psi}_{c\gamma k}(\boldsymbol{x}, t), \tag{15}$$

where $\Gamma_{\alpha i\beta j\gamma k}$ is the set of complex-valued coefficients from Sec. II B for each operator. The two-point function at zero momentum, allowing different operators Ω_Γ and $\Omega_{\Gamma'}$ at sink and source, is then defined as

$$\begin{aligned}
C_{\Gamma,\Gamma'}(t - t') &= \sum_{\boldsymbol{x}}\langle\Omega_\Gamma(\boldsymbol{x}, t)\Omega^\dagger_{\Gamma'}(\boldsymbol{x}', t')\rangle\\
&= \sum_{\boldsymbol{x}}\Gamma_{\alpha i\beta j\gamma k}\epsilon_{abc}\Gamma'^*_{\bar{\alpha}\bar{i}\bar{\beta}\bar{j}\bar{\gamma}\bar{k}}\epsilon_{\bar{a}\bar{b}\bar{c}}\langle\tilde{\psi}_{a\alpha i}(\boldsymbol{x}, t)\\
&\quad\times\tilde{\psi}_{b\beta j}(\boldsymbol{x}, t)\tilde{\psi}_{c\gamma k}(\boldsymbol{x}, t)\tilde{\psi}^\dagger_{\bar{a}\bar{\alpha}\bar{i}}(\boldsymbol{x}', t')\\
&\quad\times\tilde{\psi}^\dagger_{\bar{b}\bar{\beta}\bar{j}}(\boldsymbol{x}', t')\tilde{\psi}^\dagger_{\bar{c}\bar{\gamma}\bar{k}}(\boldsymbol{x}', t')\rangle,
\end{aligned} \tag{16}$$

where the brackets denote the Euclidean path integral over the gauge fields and fermions, weighted with e^{-S}. The path integral over the fermions can be performed explicitly, giving heavy-quark propagators and determinants of the Dirac operators for all quark flavors. Following Ref. [43], we define three-quark propagators (for a given gauge field U) that have been color contracted and summed over $\boldsymbol{x}$:

$$\begin{aligned}
\tilde{G}^{(3)}_{\alpha i\bar{\alpha}\bar{i}\beta j\bar{\beta}\bar{j}\gamma k\bar{\gamma}\bar{k}}(t, t', \boldsymbol{x}') &= \sum_{\boldsymbol{x}}\epsilon_{abc}\epsilon_{\bar{a}\bar{b}\bar{c}}\tilde{G}_{a\alpha i\bar{a}\bar{\alpha}\bar{i}}(\boldsymbol{x}, t, \boldsymbol{x}', t')\\
&\quad\times\tilde{G}_{b\beta j\bar{b}\bar{\beta}\bar{j}}(\boldsymbol{x}, t, \boldsymbol{x}', t')\\
&\quad\times\tilde{G}_{c\gamma k\bar{c}\bar{\gamma}\bar{k}}(\boldsymbol{x}, t, \boldsymbol{x}', t'),
\end{aligned} \tag{17}$$

where $\tilde{G}_{a\alpha i\bar{a}\bar{\alpha}\bar{i}}(\boldsymbol{x}, t, \boldsymbol{x}', t')$ denotes a heavy-quark propagator with smearing and, depending on i and $\bar{i}$, derivatives at the source and sink. Performing the fermionic path integral in Eq. (16) gives six contractions because all three heavy-quark flavors are equal. Using the antisymmetry of the epsilon tensor, one obtains

$$\begin{aligned}
C_{\Gamma,\Gamma'}(t - t') = \Gamma_{\alpha i\beta j\gamma k}\Gamma'^*_{\bar{\alpha}\bar{i}\bar{\beta}\bar{j}\bar{\gamma}\bar{k}}\langle&\tilde{G}^{(3)}_{\alpha i\bar{\alpha}\bar{i}\beta j\bar{\beta}\bar{j}\gamma k\bar{\gamma}\bar{k}}(t, t', \boldsymbol{x}') + \tilde{G}^{(3)}_{\alpha i\bar{\beta}\bar{j}\beta j\bar{\gamma}\bar{k}\gamma k\bar{\alpha}\bar{i}}(t, t', \boldsymbol{x}') + \tilde{G}^{(3)}_{\alpha i\bar{\gamma}\bar{k}\beta j\bar{\alpha}\bar{i}\gamma k\bar{\beta}\bar{j}}(t, t', \boldsymbol{x}')\\
&+ \tilde{G}^{(3)}_{\alpha i\bar{\beta}\bar{j}\beta j\bar{\alpha}\bar{i}\gamma k\bar{\gamma}\bar{k}}(t, t', \boldsymbol{x}') + \tilde{G}^{(3)}_{\alpha i\bar{\gamma}\bar{k}\beta j\bar{\beta}\bar{j}\gamma k\bar{\alpha}\bar{i}}(t, t', \boldsymbol{x}') + \tilde{G}^{(3)}_{\alpha i\bar{\alpha}\bar{i}\beta j\bar{\gamma}\bar{k}\gamma k\bar{\beta}\bar{j}}(t, t', \boldsymbol{x}')\rangle_U.
\end{aligned} \tag{18}$$

Here, $\langle\ldots\rangle_U$ denotes the path integral over the gauge fields U only, where the weighting factor is given by $e^{-S_{\text{gauge}}} \times$ (fermion determinants).

In the numerical calculations, performing all the multiplications in the three-quark propagator (17) is expensive, and it is important to use symmetries to reduce the number of operations needed. Defining multi-indices $I = (\alpha i\bar{\alpha}\bar{i})$, $J = (\beta j\bar{\beta}\bar{j})$, and $K = (\gamma k\bar{\gamma}\bar{k})$, one finds that $\tilde{G}^{(3)}_{IJK}$ is totally symmetric in I, J, K. Furthermore, since the baryon operators constructed in the previous two sections contain at most two derivatives total, only those components of $\tilde{G}^{(3)}_{\alpha i\bar{\alpha}\bar{i}\beta j\bar{\beta}\bar{j}\gamma k\bar{\gamma}\bar{k}}$ with

$$\begin{aligned}
n_D(i) + n_D(j) + n_D(k) &\le 2,\\
n_D(\bar{i}) + n_D(\bar{j}) + n_D(\bar{k}) &\le 2
\end{aligned} \tag{19}$$

are needed [$n_D(i)$ denotes the number of derivatives associated with the index i; see Eq. (14)].

III. LATTICE ACTIONS AND PARAMETERS

The path integral over the gauge fields U in Eq. (18) is performed by averaging over samples of lattice gauge-field configurations. The configurations used here have been generated by the RBC/UKQCD Collaboration [37] and

TABLE III. Summary of lattice parameters. The coupling in the Iwasaki gauge action is given as $\beta = 6/g^2$, and $am_{u,d}$, am_s are the bare masses of the domain-wall sea quarks. The parameters am_b, u_{0L}, c_3, and c_4 enter in the NRQCD action for the b quarks. The lattice spacings a were computed in Ref. [36]. The molecular dynamics (MD) range specifies the range of the gauge-field generation Markov chain [37] for which "measurements" are performed. The measurements are separated by the given step size in MD time and are done for $n_{\rm src}$ different source locations [$(\boldsymbol{x}', t')$ in Eq. (16)] on each gauge-field configuration.

$L^3 \times T$	β	$am_{u,d}$	am_s	am_b	u_{0L}	c_3	c_4	MD range, step	$n_{\rm src}$	a (fm)	m_π (GeV)
$24^3 \times 64$	2.13	0.005	0.04	2.487	0.8439	1.196	1.168	900–8660, 10	32	0.1119(17)	0.3377(54)
$24^3 \times 64$	2.13	0.01	0.04	2.522	0.8439	1.196	1.168	1480–8520, 10	32	0.1139(19)	0.4194(70)
$24^3 \times 64$	2.13	0.02	0.04	2.622	0.8433	1.196	1.168	1800–3600, 10	32	0.1177(29)	0.541(14)
$24^3 \times 64$	2.13	0.03	0.04	2.691	0.8428	1.196	1.168	1280–3060, 10	32	0.1196(29)	0.641(15)
$32^3 \times 64$	2.25	0.004	0.03	1.831	0.8609	1.175	1.113	580–6840, 10	24	0.0849(12)	0.2950(40)
$32^3 \times 64$	2.25	0.006	0.03	1.829	0.8609	1.175	1.113	552–7632, 16	24	0.0848(17)	0.3529(69)
$32^3 \times 64$	2.25	0.008	0.03	1.864	0.8608	1.175	1.113	540–5920, 10	24	0.0864(12)	0.3950(55)

include dynamical u, d, and s quarks, with $m_u = m_d$. These quarks were implemented with a domain-wall action [38–40], which is a five-dimensional action that leads to an approximate lattice chiral symmetry for the four-dimensional theory. This chiral symmetry becomes exact when the length of the auxiliary fifth dimension is taken to infinity. For the gauge action, the Iwasaki discretization [45,46] is used (the gauge fields are four dimensional, i.e. constant in the five-direction). The domain-wall formalism requires additional Pauli-Villars fields to cancel bulk modes [39,47], so that the gauge fields U are distributed with probability density proportional to

$$\frac{\det[K^{\rm DW}(U; aM_5, am_{u,d})]^2 \det[K^{\rm DW}(U; aM_5, am_s)]}{\det[K^{\rm DW}(U; aM_5, 1)]^3} \times e^{-S_{\rm gauge}[U]}, \tag{20}$$

where $K^{\rm DW}(U; aM_5, am)$ is the five-dimensional domain-wall operator with domain-wall height M_5 and quark mass m. Seven ensembles of gauge fields with different parameters are included in the analysis, as shown in Table III. There are ensembles with two different values of the gauge coupling $\beta = 6/g^2$, leading to lattice spacings of $a \approx 0.11$ fm and $a \approx 0.085$ fm. The number of lattice points is chosen to be $24^3 \times 64$ and $32^3 \times 64$, respectively, so that the spatial volume in physical units is equal to about $(2.7\ \text{fm})^3$ in both cases.

The lattice NRQCD action for the b quarks has the same form as in Ref. [36]. It can be written as

$$S_\psi = a^3 \sum_{\boldsymbol{x},t} \psi^\dagger(\boldsymbol{x}, t)[\psi(\boldsymbol{x}, t) - K(t)\psi(\boldsymbol{x}, t-a)], \tag{21}$$

where ψ is a two-component spinor, and $K(t)$ is given by [35]

$$K(t) = \left(1 - \frac{a\delta H|_t}{2}\right)\left(1 - \frac{aH_0|_t}{2n}\right)^n U_4^\dagger(t-a) \times \left(1 - \frac{aH_0|_{t-a}}{2n}\right)^n \left(1 - \frac{a\delta H|_{t-a}}{2}\right), \tag{22}$$

with the leading-order kinetic energy operator,

$$H_0 = -\frac{\Delta^{(2)}}{2m_b}, \tag{23}$$

and the following higher-order relativistic and discretization corrections:

$$\begin{aligned}\delta H = &-c_1 \frac{(\Delta^{(2)})^2}{8m_b^3} + c_2 \frac{ig}{8m_b^2}(\boldsymbol{\nabla}\cdot\tilde{\boldsymbol{E}} - \tilde{\boldsymbol{E}}\cdot\boldsymbol{\nabla}) \\ &- c_3 \frac{g}{8m_b^2}\boldsymbol{\sigma}\cdot(\tilde{\boldsymbol{\nabla}}\times\tilde{\boldsymbol{E}} - \tilde{\boldsymbol{E}}\times\tilde{\boldsymbol{\nabla}}) - c_4 \frac{g}{2m_b}\boldsymbol{\sigma}\cdot\tilde{\boldsymbol{B}} \\ &+ c_5 \frac{a^2\Delta^{(4)}}{24m_b} - c_6 \frac{a(\Delta^{(2)})^2}{16nm_b^2} - c_7 \frac{g}{8m_b^3}\{\Delta^{(2)}, \boldsymbol{\sigma}\cdot\tilde{\boldsymbol{B}}\} \\ &- c_8 \frac{3g}{64m_b^4}\{\Delta^{(2)}, \boldsymbol{\sigma}\cdot(\tilde{\boldsymbol{\nabla}}\times\tilde{\boldsymbol{E}} - \tilde{\boldsymbol{E}}\times\tilde{\boldsymbol{\nabla}})\} \\ &- c_9 \frac{ig^2}{8m_b^3}\boldsymbol{\sigma}\cdot(\tilde{\boldsymbol{E}}\times\tilde{\boldsymbol{E}}).\end{aligned} \tag{24}$$

Here, $\boldsymbol{E}$ and $\boldsymbol{B}$ are the chromoelectric and chromomagnetic components of a lattice gluon field strength tensor. Unlike in the previous sections, the tilde appearing on some of the quantities in Eq. (24) does not denote smearing; instead it denotes improvement corrections which reduce discretization errors [35]. The action is also tadpole improved [48], with the values of the Landau gauge mean link u_{0L} as given in Table III. The heavy-quark masses in lattice units, am_b, are set to the physical values as determined for the same gauge-field ensembles in Ref. [36].

In Eq. (24), the terms with matching coefficients c_1, c_2, c_3, and c_4 are the relativistic corrections of order v^4. The terms with coefficients c_5 and c_6 are spatial and temporal discretization improvements for H_0. Finally, the terms with coefficients c_7, c_8, and c_9 are the spin-dependent order-v^6 terms. In principle, additional operators containing four (or more) quark fields are introduced through gluon loops, but these are not included here.

At tree level in the matching of NRQCD to QCD, the coefficients c_i in Eq. (24) are all equal to 1. Because the terms in δH are suppressed relative to H_0 by at least one power of v^2, using the tree-level values for c_i already

provides accuracy of order $\alpha_s v^2 \approx 0.02$ for the radial and orbital energy splittings in the $b\bar{b}$ and bbb systems. However, spin splittings first arise through the operators with coefficients c_3 and c_4, and therefore these two coefficients are tuned nonperturbatively here. The tuning condition used here is that, when calculated with the lattice NRQCD action, the following two combinations of bottomonium $1P$ energy levels agree with experiment:

$$-2E(\chi_{b0}) - 3E(\chi_{b1}) + 5E(\chi_{b2}), \tag{25}$$

$$-2E(\chi_{b0}) + 3E(\chi_{b1}) - E(\chi_{b2}). \tag{26}$$

As discussed in Ref. [49] and confirmed numerically in Ref. [36], to a good approximation the combination (25) is proportional to c_3, while (26) is proportional to c_4^2. Table VII of Ref. [36] gives numerical results for (25) and (26), computed with $c_i = 1$ for the same order-v^6 NRQCD action on the same gauge-field ensembles. Using these results, one can then solve for c_3 and c_4 so that the experimental values [50] for (25) and (26) are reproduced:

$$c_3 = \begin{cases} 1.196 \pm 0.106, & a \approx 0.11 \text{ fm} \\ 1.175 \pm 0.084, & a \approx 0.08 \text{ fm}, \end{cases}$$
$$c_4 = \begin{cases} 1.168 \pm 0.081, & a \approx 0.11 \text{ fm} \\ 1.113 \pm 0.053, & a \approx 0.08 \text{ fm}. \end{cases} \tag{27}$$

In the present work, the main calculations of the bbb spectrum are performed directly at c_3 and c_4 set equal to the central values in Eq. (27), and with $c_1 = c_2 = c_5 = c_6 = c_7 = c_8 = c_9 = 1$. The uncertainties in (27) are mainly statistical, and the resulting uncertainties in the bbb spectrum will be included in the final results (Sec. V).

IV. FITS OF THE TWO-POINT FUNCTIONS AND ANGULAR MOMENTUM IDENTIFICATION

The two-point functions defined in Eq. (16) are labeled by Γ and Γ', which determine the baryon interpolating operators at the sink and source, respectively. The two-point functions vanish when Γ and Γ' correspond to different irreducible representations (irreps) of the double-cover octahedral group, or when Γ and Γ' correspond to different rows of the same irrep. In the remaining cases of equal irrep and equal row at source and sink, one can average over the different rows. In the following, we use the notation $\Lambda_r^{(i)}$ for row r of the ith operator in irrep Λ, according to Table II. Then the row-averaged two-point functions are defined as

$$C_{ij}^{(\Lambda)}(t - t') = \frac{1}{\dim(\Lambda)} \sum_{r=1}^{\dim(\Lambda)} C_{\Lambda_r^{(i)}, \Lambda_r^{(j)}}(t - t'). \tag{28}$$

For the operators in Table II, one obtains a (7×7) matrix of two-point functions in the H_g irrep, (3×3) matrices in the G_{1g} and G_{2g} irreps, and (1×1) "matrices" in the H_u and G_{1u} irreps. The magnitudes of the rescaled two-point functions $|C_{ij}^{(\Lambda)}|/\sqrt{C_{ii}^{(\Lambda)} C_{jj}^{(\Lambda)}}$ at one time slice are shown in Figs. 1–3, for the H_g, G_{1g}, and G_{2g} irreps, respectively. The first important observation is that cross correlations between operators subduced from continuum operators that differ in *at least one of* the quantum numbers L, S, or J are small. Note that J is an exactly conserved quantum number in the continuum, but L and S are not. The weak coupling between operators subduced from different J values indicates that rotational symmetry breaking by the lattice is small. This has also been observed in Ref. [33] for light baryons. On the other hand, the weak coupling between operators subduced from common J values but different L or S values is a new feature appearing here. Because of the large mass of the b quarks, the dynamics is approximately nonrelativistic, and the spin-orbit coupling is suppressed, so that L and S are approximately conserved. In fact, for the lattice spacings considered here, the operator overlaps between different L or S values appear to be smaller than that between different J values. Furthermore, the overlaps between operators subduced from different J values (for example, between $H_g^{(3)}$ and $H_g^{(5)}$, which are subduced from $J = \frac{3}{2}$ and $J = \frac{7}{2}$, respectively) appear to be somewhat larger than what was seen for light baryons in Ref. [33]. This may be a consequence of the much smaller physical extent of the bbb baryons [as modeled by the initial smearing width of $r_S \approx 0.14$ fm in Eq. (11)], which makes the operators more sensitive to the nonzero lattice spacing.

As can be seen in Fig. 1, there is a strong overlap between the $H_g^{(1)}$ and $H_g^{(2)}$ operators, because both are subduced from continuum operators with the common quantum numbers $L = 0$, $S = \frac{3}{2}$, $J = \frac{3}{2}$. All other cross correlations, also in the G_{1g} and G_{2g} irreps (Figs. 2 and 3) are small, because there is suppression as a consequence of different J, L, or S.

Further information can be gained by looking at the lattice-spacing dependence of the operator overlaps. In each of the figures, the left plot shows data from $a \approx 0.11$ fm, while the right plot shows data from $a \approx 0.08$ fm. It can be seen that the cross correlations between operators subduced from different continuum J are smaller at the finer lattice spacing, demonstrating the improvement of rotational symmetry as a is reduced. On the other hand, the overlaps between $H_g^{(3)}$ and $H_g^{(1)}$, as well as between $H_g^{(3)}$ and $H_g^{(2)}$, are not smaller at the finer lattice spacing. In that case, the operators are all subduced from the same $J(= \frac{3}{2})$, and one does not expect the cross correlations to vanish in the continuum limit.

In this work, the matrix two-point functions in each irrep Λ were fitted directly using the form

$$C_{ij}^{(\Lambda)}(t - t') = \sum_{n=1}^{N} A_{n,i}^{(\Lambda)} A_{n,j}^{(\Lambda)} e^{-E_n^{(\Lambda)}(t - t')}. \tag{29}$$

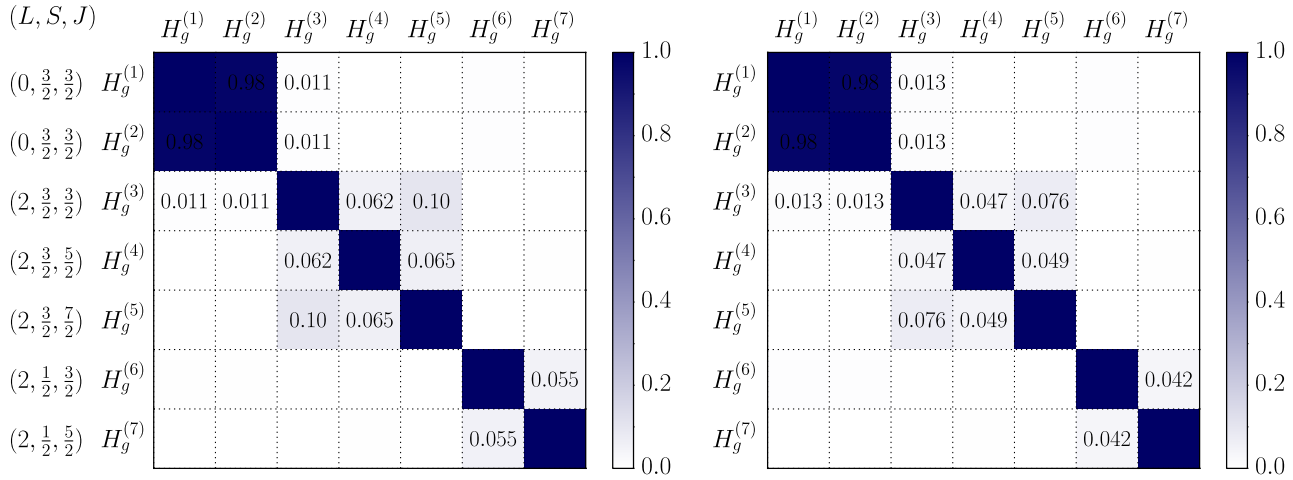

FIG. 1 (color online). Visualization of rescaled matrix two-point functions $|C_{ij}|/\sqrt{C_{ii}C_{jj}}$ in the H_g irreducible representation, at one time slice. Off-diagonal entries larger than 0.01 are also given numerically (the $i = 1$, $j = 2$ entry is 0.98). The values of L, S, and J from which each operator $H_g^{(i)}$ was subduced are indicated. Left plot: $a \approx 0.11$ fm, $am_{u,d} = 0.005$, $(t - t')/a = 5$. Right plot: $a \approx 0.08$ fm, $am_{u,d} = 0.004$, $(t - t')/a = 6$.

The number of exponentials was chosen to be equal to the dimension of the matrix, i.e. equal to the number of interpolating operators for each irrep: $N = 7$ for H_g, $N = 3$ for G_{1g} and G_{2g}, and $N = 1$ for H_u and G_{1u}. Of course, the complete spectral decomposition of the two-point functions also contains an infinite number of higher-energy exponentials. Therefore, only the data with $t - t' \geq t_{\text{min}}$ with sufficiently large t_{min} were included in the fit, so the contributions from these higher states are negligible. The dependence of the results on t_{min} will be discussed later.

The fits performed here fully take into account the statistical correlations between all data points. The dimension of the data correlation matrix for an $(N \times N)$ matrix fit is equal to $N_t N^2$, where N_t is the number of time slices included in the fit ($N_t = t_{\text{max}}/a - t_{\text{min}}/a + 1$). The definition of χ^2 contains the inverse of this data correlation matrix, and one has to make sure that the number of measurements used to estimate the data correlation matrix is much larger than its dimension. Because the number of measurements was of order $n_{\text{src}} \times n_{\text{cfg}} \sim 10^4$ for each ensemble, these large, fully correlated matrix fits were possible here (for sufficiently small N_t). In order to reduce the dimension of the data correlation matrix to $N_t N(N + 1)/2$ and thereby allow slightly larger N_t, the symmetry of the data in i, j (which is exact for infinite statistics) was used. The data for the two-point functions were first symmetrized explicitly measurement by measurement, and then the fits using Eq. (29) were performed only for $i \geq j$.

Within each irrep Λ, the operators $\Lambda^{(i)}$ in Table II are labeled by i such that they are ordered by the energy of the state with which they have the strongest overlap (this ordering was not known *a priori* and was only assigned after some initial fits). For each irrep Λ, the amplitudes in Eq. (29) are then rewritten as follows:

$$A_{n,i}^{(\Lambda)} = \begin{cases} A_i^{(\Lambda)} & \text{for } n = i \\ B_{n,i}^{(\Lambda)} A_i^{(\Lambda)} & \text{for } n \neq i, \end{cases} \tag{30}$$

using the new parameters $A_i^{(\Lambda)}$ and $B_{n,i}^{(\Lambda)}$ instead of $A_{n,i}^{(\Lambda)}$ in the fits. The parameters $B_{n,i}^{(\Lambda)}$ then describe the overlaps of the operator $\Lambda^{(i)}$ with the other states $n \neq i$, relative to the state with $n = i$.

Furthermore, the energies $E_n^{(\Lambda)}$ in Eq. (29) were rewritten for $n > 1$ as

$$\begin{aligned} E_n^{(\Lambda)} &= E_1^{(\Lambda)} + \delta_1^{(\Lambda)} + \ldots + \delta_{n-1}^{(\Lambda)}, \quad \text{with} \\ \delta_n^{(\Lambda)} &= E_{n+1}^{(\Lambda)} - E_n^{(\Lambda)}, \end{aligned} \tag{31}$$

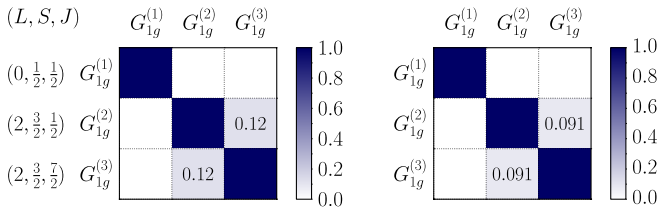

FIG. 2 (color online). Like Fig. 1, but for the G_{1g} irreducible representation.

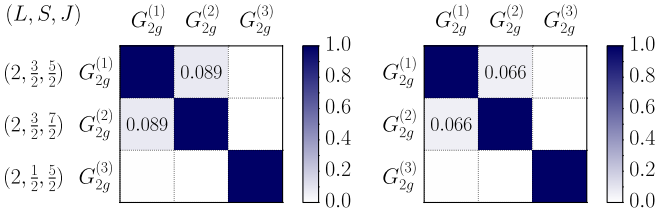

FIG. 3 (color online). Like Fig. 1, but for the G_{2g} irreducible representation.

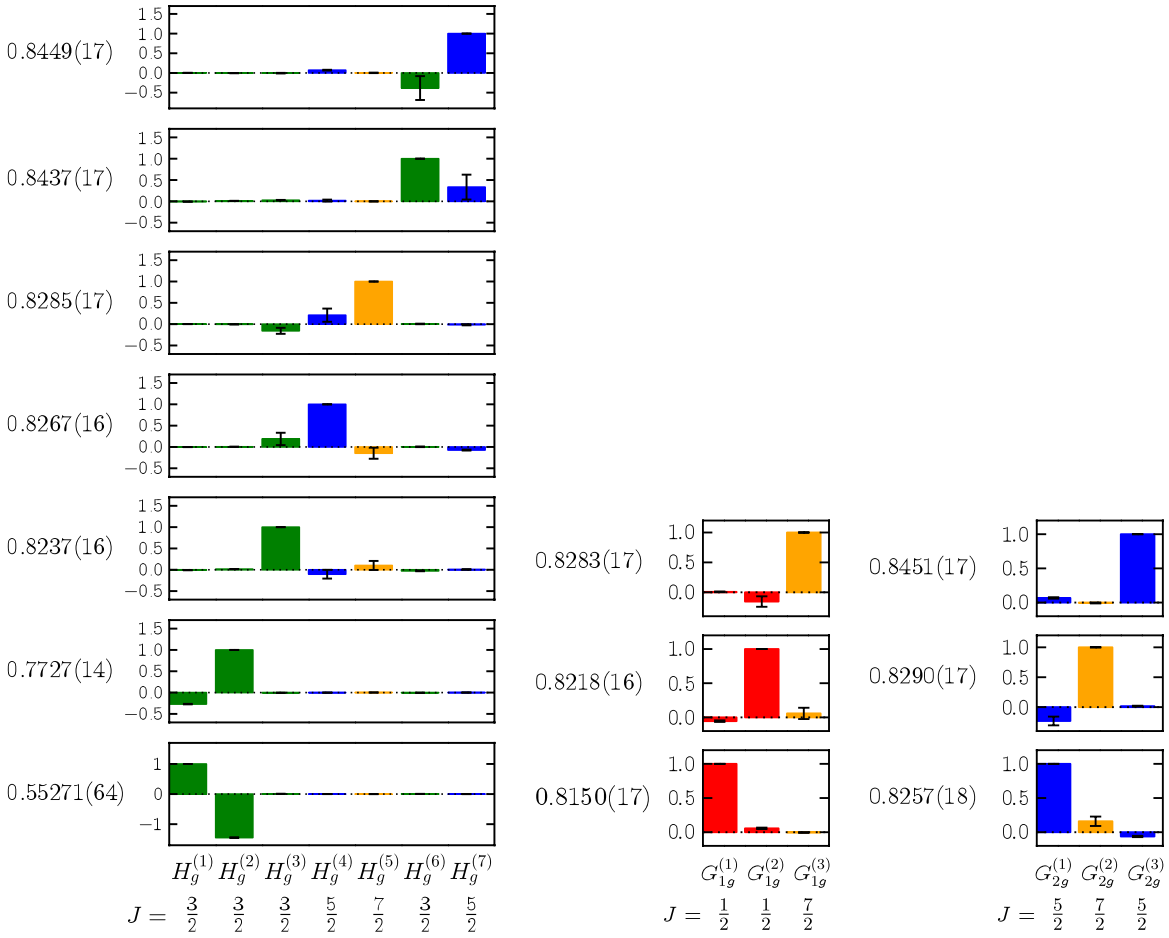

FIG. 4 (color online). Fitted energies $E_n^{(\Lambda)}$ (in lattice units; from bottom to top: $n = 1, \ldots, N$), together with histograms of the corresponding relative overlap factors $A_{n,i}^{(\Lambda)}/A_i^{(\Lambda)}$ [see Eqs. (29) and (30)]. The fits for the three different irreps were performed independently. For each i, the continuum angular momentum J from which the operator $\Lambda^{(i)}$ was subduced is given at the bottom. These values of J are also indicated by the colors in the histograms (red: $J = \frac{1}{2}$; green: $J = \frac{3}{2}$; blue: $J = \frac{5}{2}$; orange: $J = \frac{7}{2}$). The data shown here are from the ensemble with $a \approx 0.08$ fm and $am_{u,d} = 0.004$; the fits have $t_{\mathrm{min}}/a = 6$.

using the ground-state energy $E_1^{(\Lambda)}$ and the energy splittings $\delta_1^{(\Lambda)}, \ldots, \delta_{N-1}^{(\Lambda)}$ (all in units of $1/a$) as the actual fit parameters. When computing $E_n^{(\Lambda)}$ (and other combinations of energy levels) from the fit results for $E_1^{(\Lambda)}$ and $\delta_1^{(\Lambda)}, \ldots, \delta_{N-1}^{(\Lambda)}$, the uncertainties were added in a fully covariant way, using the parameter covariance matrix obtained from the second derivatives of χ^2.

Following Ref. [33], the spectral overlaps $A_{n,i}^{(\Lambda)}$ are used here to assign values of the continuum angular momentum J to each energy level $E_n^{(\Lambda)}$. Examples of fitted energies $E_n^{(\Lambda)}$, together with the relative overlap factors $A_{n,i}^{(\Lambda)}/A_i^{(\Lambda)}$, are shown in Fig. 4 for the H_g, G_{1g}, and G_{2g} irreps (in the cases of the G_{1u} and H_u irreps, there is only one operator each, subduced trivially from $J = \frac{1}{2}$ and $J = \frac{3}{2}$, respectively). The angular momentum identification proceeds as follows: for each energy level $E_n^{(\Lambda)}$, the operator $\Lambda^{(i)}$ with the largest relative overlap factor $A_{n,i}^{(\Lambda)}/A_i^{(\Lambda)}$ is determined. The value of J from which this operator was subduced is then assigned to this energy level. As can be seen in Fig. 4, no ambiguity arises here. Notice that the two $J = \frac{5}{2}$ levels appearing in the H_g irrep also show up in the G_{2g} irrep, with nearly identical energies. Similarly, the $J = \frac{7}{2}$ level appears in all three irreps H_g, G_{1g}, and G_{2g}, again with nearly identical energies. For these levels, the absolute overlap factors were also found to be consistent across the different irreps, confirming the assignment of J.

Because of the strong statistical correlations across irreps, the tiny splittings of the $J = \frac{5}{2}$ and $J = \frac{7}{2}$ levels into the different lattice irreps, which are caused by rotational symmetry breaking, can be computed with smaller uncertainties than the individual energies of these levels. To this end, simultaneous fits of the two-point functions in the H_g, G_{1g}, and G_{2g} irreps were performed, where a global correlated χ^2 was formed but all fit parameters remained independent for each irrep. The results for the rotational-symmetry-breaking-induced energy splittings, converted

TABLE IV. Splitting of continuum energy levels with $J > \frac{3}{2}$ into different irreducible representations of the double-cover octahedral group. All results are in MeV. The data at $a \approx 0.11$ fm are from the ensemble with $am_{u,d} = 0.005$, while the data at $a \approx 0.08$ fm are from the ensemble with $am_{u,d} = 0.004$.

Continuum J^P	Splitting	$a \approx 0.11$ fm	$a \approx 0.08$ fm
$\frac{5}{2}^+$	$E_4^{(H_g)} - E_1^{(G_{2g})}$	5.8(2.0)	2.5(2.0)
$\frac{5}{2}^+$	$E_3^{(G_{2g})} - E_7^{(H_g)}$	0.70(44)	0.44(64)
$\frac{7}{2}^+$	$E_2^{(G_{2g})} - E_3^{(G_{1g})}$	2.1(1.1)	1.6(1.4)
$\frac{7}{2}^+$	$E_5^{(H_g)} - E_3^{(G_{1g})}$	1.49(78)	0.38(79)
$\frac{7}{2}^+$	$E_2^{(G_{2g})} - E_5^{(H_g)}$	0.59(45)	1.24(72)

to MeV, are given in Table IV for two gauge-field ensembles. Up to some statistical fluctuations, the splittings are smaller at $a \approx 0.08$ fm compared to $a \approx 0.11$ fm, consistent with the discretization errors proportional to $\alpha_s a^2$ that are expected for the improved lattice NRQCD action used here. Along with the behavior of the off-diagonal matrix elements that was discussed at the beginning of this section, the results shown in Table IV provide another demonstration of the improvement of rotational symmetry when the lattice spacing a is reduced.

Finally, to get the best possible estimates of the continuum energy levels, new simultaneous fits of the two-point functions in the H_g, G_{1g}, and G_{2g} irreps were performed, in which the fitted energies for the matching $J = \frac{5}{2}$ and $J = \frac{7}{2}$ levels in different irreps were forced to be equal:

$$E_4^{(H_g)} = E_1^{(G_{2g})}, \qquad E_7^{(H_g)} = E_3^{(G_{2g})}, \qquad E_5^{(H_g)} = E_3^{(G_{1g})} = E_2^{(G_{2g})}. \tag{32}$$

This was implemented by augmenting the χ^2 function of the simultaneous fit in the following way:

$$\chi^2 \to \chi^2 + [E_4^{(H_g)} - E_1^{(G_{2g})}]^2/\sigma^2 + [E_7^{(H_g)} - E_3^{(G_{2g})}]^2/\sigma^2 + [E_5^{(H_g)} - E_3^{(G_{1g})}]^2/\sigma^2 + [E_3^{(G_{1g})} - E_2^{(G_{2g})}]^2/\sigma^2, \tag{33}$$

where the energies $E_n^{(\Lambda)}$ are expressed in terms of the actual fit parameters as $E_n^{(\Lambda)} = E_1^{(\Lambda)} + \delta_1^{(\Lambda)} + \ldots + \delta_{n-1}^{(\Lambda)}$. The width σ in Eq. (33) was chosen about 2 orders of magnitude smaller than the typical statistical uncertainty in the energies. By minimizing the augmented χ^2, fit parameters are returned that satisfy the conditions (32) up to the input width σ. These new fits still had $\chi^2/\text{d.o.f} \approx 1$, because of the smallness of the energy splittings between the different irreps. Performing the simultaneous fit with the enforced relations (32) also stabilizes the extraction of the very close energy levels (such as $E_6^{(H_g)}$ and $E_7^{(H_g)}$) and makes the spectral overlap factors more sharply peaked, as can be seen in Fig. 5. Note that in this work no further constraints beyond that of Eq. (33) were imposed on any of the fit parameters.

These simultaneous fits, along with simple one-exponential fits in the H_u and G_{1u} irreps, yield 11 different bbb energy levels. Having performed the angular momentum identification, these levels can now be labeled by J^P and a new subscript counting the states in each J^P channel by increasing energy:

$$\begin{aligned} &E_1(\tfrac{1}{2}^+), \quad E_2(\tfrac{1}{2}^+), \quad E_1(\tfrac{3}{2}^+), \quad E_2(\tfrac{3}{2}^+), \\ &E_3(\tfrac{3}{2}^+), \quad E_4(\tfrac{3}{2}^+), \quad E_1(\tfrac{5}{2}^+), \quad E_2(\tfrac{5}{2}^+), \\ &E_1(\tfrac{7}{2}^+), \quad E_1(\tfrac{1}{2}^-), \quad E_1(\tfrac{3}{2}^-). \end{aligned} \tag{34}$$

Because NRQCD is used in this work, the extracted energies do not include the rest masses of the three b quarks; i.e. they are all shifted by a common amount that is not known with sufficient precision. Therefore, only energy *differences* are considered in the following.

The remaining point to be discussed in this section is the choice of t_{min}, the starting time slice from which the fits are performed. This parameter has to be chosen large enough such that the contamination from higher-excited states, which decay exponentially with t, is negligible. However, t_{min} must not be made too large either, as the statistical uncertainties increase with t_{min} and the fits eventually become unstable. Figures 6 and 7 show the t_{min} dependence of the set of ten independent energy splittings chosen here. For the matrix two-point functions in the H_g, G_{1g}, and G_{2g} irreps, the total number of time slices included in the fit, $N_t = t_{\text{max}}/a - t_{\text{min}}/a + 1$, was held constant as t_{min} was varied, to keep the dimension of the data correlation matrix fixed at a manageable size ($N_t = 5$, 8, 8 for the H_g, G_{1g}, G_{2g} irreps, respectively).

As can be seen in Figs. 6 and 7, for the energy splittings $aE_1(\frac{3}{2}^-) - aE_1(\frac{3}{2}^+)$, $aE_2(\frac{3}{2}^+) - aE_1(\frac{3}{2}^+)$, and $aE_1(\frac{7}{2}^+) - aE_1(\frac{3}{2}^+)$, which are large energy differences between bbb states of rather different spatial structure, the plateaus set in later than for the other, smaller splittings, which mainly constitute the fine and hyperfine structures. To extract the best possible estimates for further analysis, at the coarse lattice spacing the three large energy splittings were taken from the fits with $t_{\text{min}}/a = 8$ or $t_{\text{min}}/a = 7$, while the other splittings were taken from $t_{\text{min}}/a = 5$. At the fine lattice spacing, $t_{\text{min}}/a = 12$ was selected for the three large

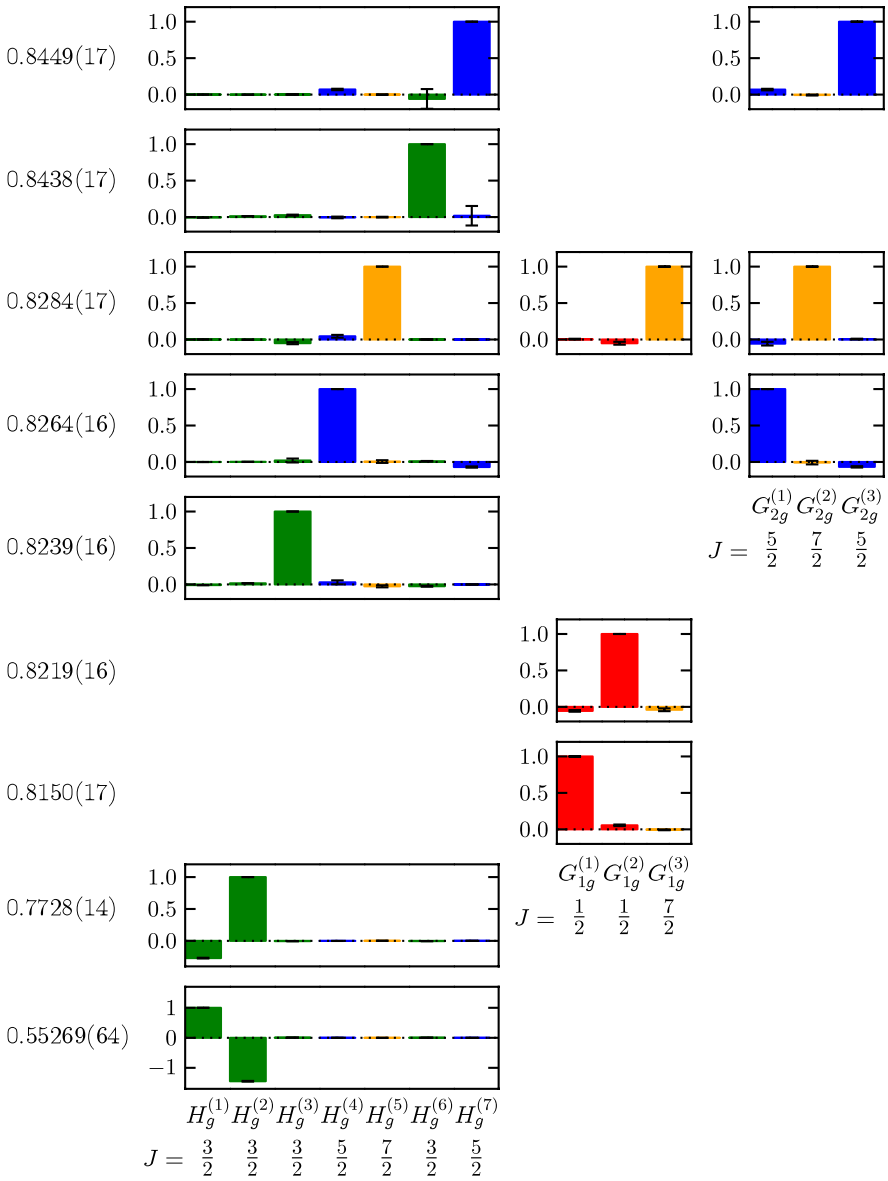

FIG. 5 (color online). Like Fig. 4, but for a coupled fit containing the H_g, G_{1g}, and G_{2g} irreps, where the equalities of common $J = \frac{5}{2}$ and $J = \frac{7}{2}$ energy levels are enforced: $E_4^{(H_g)} = E_1^{(G_{2g})}$, $E_7^{(H_g)} = E_3^{(G_{2g})}$, and $E_5^{(H_g)} = E_3^{(G_{1g})} = E_2^{(G_{2g})}$.

splittings, and $t_{\mathrm{min}}/a = 6$ for all other splittings. Possible remaining systematic uncertainties resulting from the choice of t_{min}/a were estimated by computing the shift in the energy splittings when reducing t_{min}/a from the selected values by one unit. These shifts were added in quadrature to the original statistical uncertainties, and the resulting total fitting uncertainties are indicated by the shaded bands in Figs. 6 and 7.

V. FINAL RESULTS FOR THE *bbb* SPECTRUM

In the previous section, ten *bbb* energy splittings were computed for each of the seven different ensembles of gauge fields. These results are given by the horizontal bands in Figs. 6 and 7. The values of the light sea-quark masses used in the generation of the gauge-field ensembles correspond to pion masses that are larger than physical (see Table III). The final step of the analysis is to perform extrapolations of the *bbb* spectrum to the physical value of the pion mass. These extrapolations are done here using the same method that was used for the bottomonium spectrum in Ref. [36]. The light quarks influence the *bbb* spectrum only through their vacuum-polarization effects, and the dependence on $m_{u,d}$ is weak. Therefore, it is sufficient to perform the extrapolations linearly in $m_{u,d}$, and hence linearly in m_π^2.

The *bbb* energy splittings were first converted to MeV using the values of the lattice spacings as given in Table III.

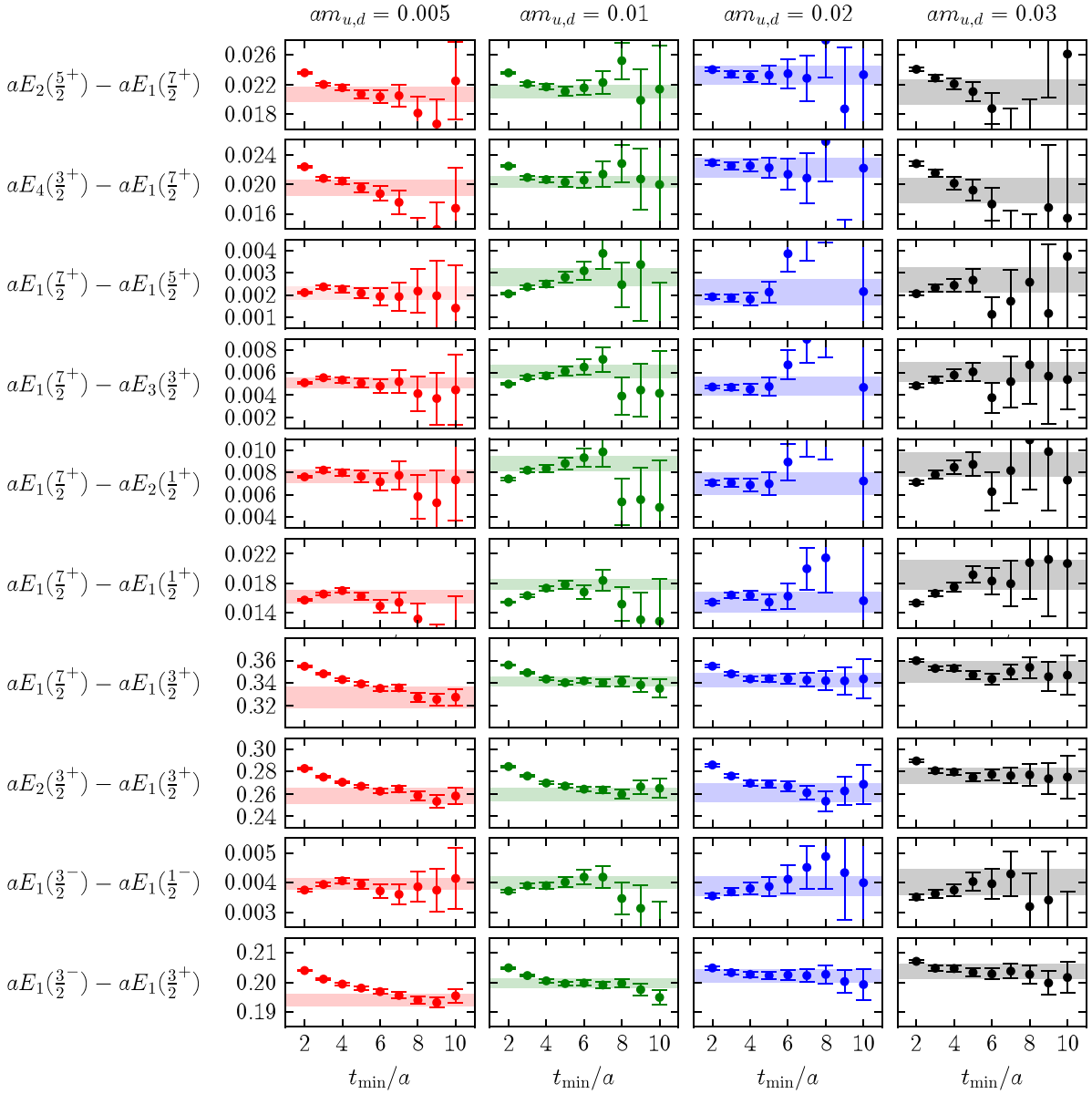

FIG. 6 (color online). Dependence of the results for the bbb energy splittings on the start time slice $t_{\rm min}$ that is used in the fit. The data shown here are for the ensembles with $a \approx 0.11$ fm, with the light-quark masses of $am_{u,d} = 0.005, 0.01, 0.02, 0.03$ (from left to right). The shaded bands indicate the best possible estimates of the energy splittings.

Then, coupled fits to the data for the two different values of the gauge coupling, $\beta_1 = 2.25$ and $\beta_2 = 2.13$, were performed using

$$E(m_\pi^2, \beta_1) = E(0, \beta_1) + Am_\pi^2,$$
$$E(m_\pi^2, \beta_2) = E(0, \beta_2) + Am_\pi^2, \tag{35}$$

where $E(m_\pi^2, \beta)$ denotes a generic bbb energy splitting. The ensembles with $\beta = \beta_1$ have $a \approx 0.08$ fm, while the ensembles with $\beta = \beta_2$ have $a \approx 0.11$ fm. The free fit parameters in Eq. (35) are $E(0, \beta_1)$, $E(0, \beta_2)$, and A. No continuum extrapolation is performed here, because lattice NRQCD is an effective field theory that requires a cutoff $a^{-1} \lesssim m_b$. The only assumption made here is that higher-order effects proportional to terms like $a^2 m_\pi^2$ are negligible, so the same parameter A can be used for both values of β.

The fits to the data for the ten bbb energy splittings using Eq. (35) are visualized in Fig. 8. Evaluating the fitted functions for $m_\pi = 138$ MeV leads to the results given in Table V. In addition to the ten independent energy splittings discussed so far, the table also gives some further combinations for convenience, in particular, the energy differences of all ten excited states to the ground state $E_1(\frac{3}{2}^+)$, and a result for the very small splitting $E_4(\frac{3}{2}^+) - E_2(\frac{5}{2}^+)$ that, as a consequence of the strong correlations,

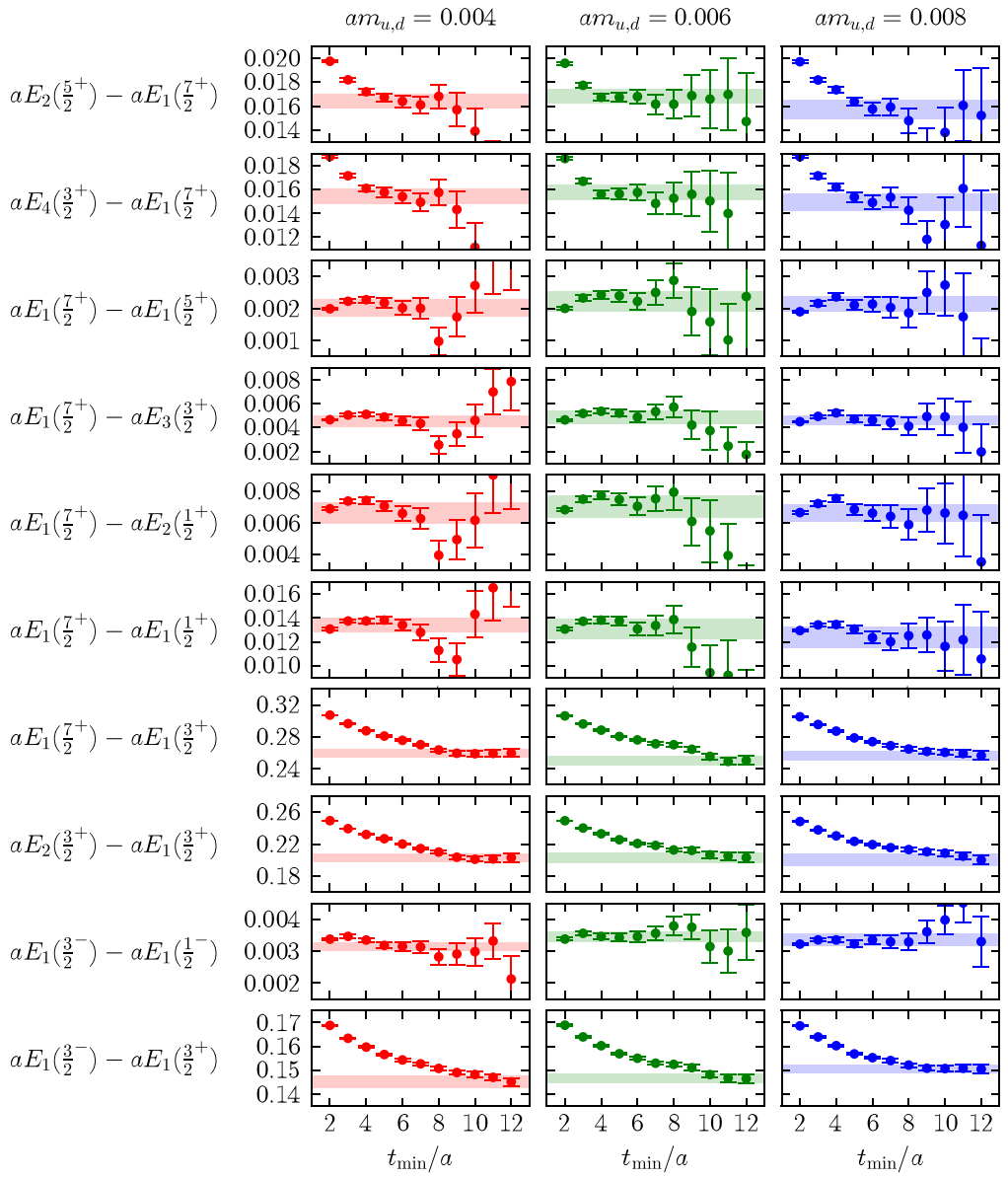

FIG. 7 (color online). Dependence of the results for the bbb energy splittings on the start time slice $t_{\rm min}$ that is used in the fit. The data shown here are for the ensembles with $a \approx 0.08$ fm, with the light-quark masses of $am_{u,d} = 0.004$, 0.006, 0.008 (from left to right). The shaded bands indicate the best possible estimates of the energy splittings.

has smaller absolute uncertainties than the other splittings involving the same levels.

As can be seen in Fig. 8 and Table V, the results for the bbb spectrum show only a weak dependence on the lattice spacing, which in most cases is not statistically significant. The results at $a \approx 0.08$ fm and $m_\pi = 138$ MeV can be quoted as the predicted values for the continuum bbb spectrum, once the remaining systematic uncertainties have been estimated. These estimates can be made using information from Sec. VI about the dependence of the bbb energy splittings on the couplings c_i in the NRQCD action [see Eq. (24)]. The systematic uncertainty is computed individually for each energy splitting E, using the formula

$$\sigma_E^{(\rm syst)} = \Bigg[\left(\frac{\partial E}{\partial c_3}\right)^2 \sigma_{c_3}^2 + \left(\frac{\partial E}{\partial c_4}\right)^2 \sigma_{c_4}^2 + (0.02 E_{\rm SI})^2 + (0.07(E - E_{\rm SI}))^2\Bigg]^{1/2}, \tag{36}$$

which takes into account the varying contributions from spin-dependent and spin-independent NRQCD interactions.

The first two terms in Eq. (36) correspond to the uncertainty in E that results from the uncertainty in the tuning of the NRQCD coefficients c_3, and c_4 [see Eq. (27)]. The derivatives with respect to c_3 and c_4 are approximated using discrete difference quotients formed from the results in the last three columns of Table VI. To save computer

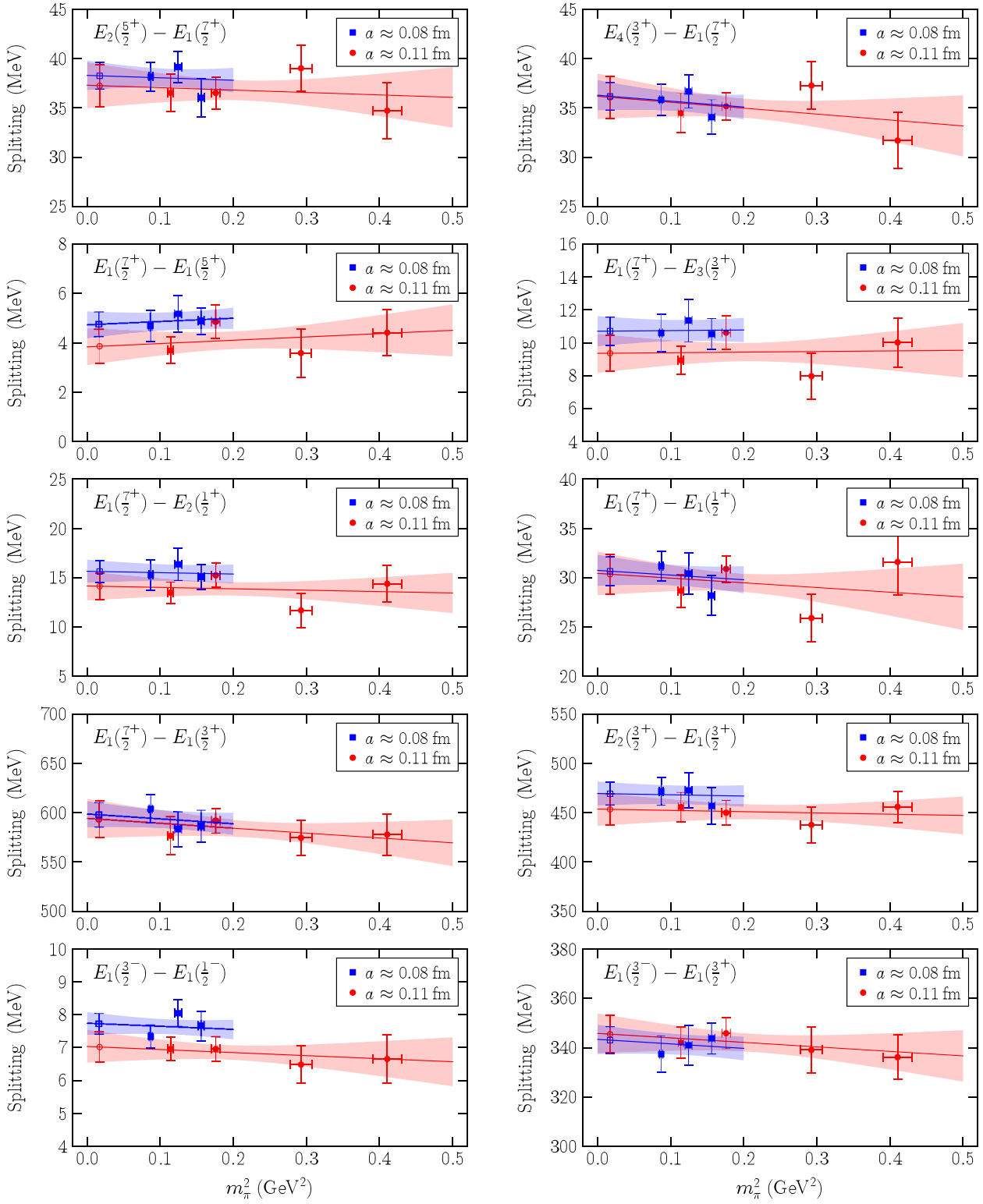

FIG. 8 (color online). Extrapolation of the bbb energy splittings to the physical pion mass. The fits are linear in m_π^2 and were done simultaneously for the data at the two different lattice spacings. The data are plotted with closed symbols, and the extrapolated results at $m_\pi = 138$ MeV are plotted with open symbols. The fitted functions and their 1-sigma uncertainty are given by the lines and the shaded regions.

TABLE V. Energy splittings in MeV between various bbb states, extrapolated to the physical pion mass. In the final results (last column), the central values and statistical/fitting/scale setting uncertainties are taken from $a \approx 0.08$ fm, and estimates of the total systematic uncertainties computed using Eq. (36) are given. The ground-state mass is equal to $E_1(\frac{3}{2}^+) = 14371 \pm 4 \pm 11$ MeV [24].

	$a \approx 0.11$ fm	$a \approx 0.08$ fm	Final result
$E_1(\frac{1}{2}^+) - E_1(\frac{3}{2}^+)$	563(21)	567(14)	$567 \pm 14 \pm 12$
$E_2(\frac{1}{2}^+) - E_1(\frac{3}{2}^+)$	579(20)	582(13)	$582 \pm 13 \pm 13$
$E_2(\frac{3}{2}^+) - E_1(\frac{3}{2}^+)$	453(16)	469(11)	$469 \pm 11 \pm 9$
$E_3(\frac{3}{2}^+) - E_1(\frac{3}{2}^+)$	584(20)	587(13)	$587 \pm 13 \pm 12$
$E_4(\frac{3}{2}^+) - E_1(\frac{3}{2}^+)$	629(21)	634(14)	$634 \pm 14 \pm 13$
$E_1(\frac{5}{2}^+) - E_1(\frac{3}{2}^+)$	589(19)	593(13)	$593 \pm 13 \pm 12$
$E_2(\frac{5}{2}^+) - E_1(\frac{3}{2}^+)$	630(21)	636(14)	$636 \pm 14 \pm 13$
$E_1(\frac{7}{2}^+) - E_1(\frac{3}{2}^+)$	593(19)	598(12)	$598 \pm 12 \pm 12$
$E_1(\frac{1}{2}^-) - E_1(\frac{3}{2}^+)$	338.4(8.0)	335.3(5.8)	$335.3 \pm 5.8 \pm 7.4$
$E_1(\frac{3}{2}^-) - E_1(\frac{3}{2}^+)$	345.5(7.5)	343.0(5.5)	$343.0 \pm 5.5 \pm 7.2$
$E_1(\frac{1}{2}^+) - E_1(\frac{7}{2}^+)$	−30.3(2.0)	−30.7(1.4)	$-30.7 \pm 1.4 \pm 0.8$
$E_2(\frac{1}{2}^+) - E_1(\frac{7}{2}^+)$	−14.1(1.4)	−15.6(1.1)	$-15.6 \pm 1.1 \pm 1.6$
$E_3(\frac{3}{2}^+) - E_1(\frac{7}{2}^+)$	−9.4(1.1)	−10.71(85)	$-10.7 \pm 0.9 \pm 1.2$
$E_4(\frac{3}{2}^+) - E_1(\frac{7}{2}^+)$	36.1(2.1)	36.2(1.4)	$36.2 \pm 1.4 \pm 1.4$
$E_1(\frac{5}{2}^+) - E_1(\frac{7}{2}^+)$	−3.86(69)	−4.75(50)	$-4.75 \pm 0.50 \pm 0.55$
$E_2(\frac{5}{2}^+) - E_1(\frac{7}{2}^+)$	37.2(2.2)	38.2(1.4)	$38.2 \pm 1.4 \pm 1.1$
$E_1(\frac{1}{2}^-) - E_1(\frac{3}{2}^-)$	−7.02(45)	−7.72(32)	$-7.72 \pm 0.32 \pm 0.90$
$E_4(\frac{3}{2}^+) - E_2(\frac{5}{2}^+)$	−1.63(62)	−2.06(48)	$-2.06 \pm 0.48 \pm 0.59$

time, the results in Table VI were obtained at the coarser lattice spacing $a \approx 0.11$ fm. However, for the purpose of estimating $\sigma_E^{(\mathrm{syst})}$, it is sufficient to approximate the derivatives with respect to c_3 and c_4 at $a \approx 0.08$ fm as being equal to those at $a \approx 0.11$ fm, and then setting $\sigma_{c_3} = 0.084$ and $\sigma_{c_4} = 0.053$ according to Eq. (27) for $a \approx 0.08$ fm.

The third term in Eq. (36) describes the systematic uncertainty in the spin-independent contribution to the energy splitting. This contribution, E_{SI}, is obtained by setting $c_3 = c_4 = c_7 = c_8 = c_9 = 0$ in the NRQCD action. Given the weak a dependence of the spectrum, E_{SI} can be taken from the second column of Table VI. However, the estimate of a 2% systematic uncertainty is specific to $a \approx 0.08$ fm. It includes the radiative, discretization, and relativistic errors, and is based on the discussion of radial and orbital energy splittings for the same lattice spacing in bottomonium [36]. The estimates of uncertainties for bottomonium are also valid for triply bottom baryons, since the energy and momentum scales involved are the same (indeed, the results of Sec. VI confirm that the v^2 expansion converges at a similar rate for the bbb system as for bottomonium).

The last term in Eq. (36) describes the systematic uncertainty in the spin-dependent contribution to the energy splitting. This contribution can be isolated by computing the difference $(E - E_{\mathrm{SI}})$, where E is the result from the full NRQCD action. Because the leading spin-dependent couplings c_3 and c_4 have been tuned nonperturbatively (and their tuning uncertainty is already taken into account), and because the spin-dependent order-v^6 terms have been included in the NRQCD action at tree level, the dominant remaining sources of error for the spin splittings are discretization errors and the missing radiative corrections in the v^6 terms. Following the discussion of the bottomonium fine and hyperfine splittings in Ref. [36], a systematic uncertainty of 7% is assigned here to the spin-dependent contributions at $a \approx 0.08$ fm. Again, the values of $(E - E_{\mathrm{SI}})$ can be taken from Table VI (the differences of the results from columns six and two), because the spectrum has a weak a dependence.

The final results for the bbb spectrum, with systematic uncertainties computed using Eq. (36), are given in the last column of Table V. The energy differences of the ten excited states to the ground state Ω_{bbb} are plotted in Fig. 9. The results for the different energy levels are highly correlated, and the small splittings between nearby states can in fact be computed with much smaller absolute uncertainties. These smaller energy splittings are given in the lower part of Table V and are plotted in Fig. 10.

TABLE VI. Dependence of the bbb spectrum on the coefficients c_i in the NRQCD action [see Eq. (24)]. All results are given in MeV. The data are from the ensemble with $a \approx 0.11$ fm and $am_{u,d} = 0.005$.

Coefficient(s)								
c_1, c_2	0	1	1	1	1	1	1	1
c_3	0	0	0	1.196	1.196	1.196	1.196	1
c_4	0	0	1.168	0	1.168	1.168	1	1.168
c_7, c_8, c_9	0	0	0	0	0	1	1	1
Splitting								
$E_1(\frac{1}{2}^+) - E_1(\frac{3}{2}^+)$	592(12)	582(11)	546(15)	559(15)	545(15)	548(21)	551(15)	548(15)
$E_2(\frac{1}{2}^+) - E_1(\frac{3}{2}^+)$	617(11)	607(10)	570(14)	572(15)	557(15)	563(20)	566(14)	565(14)
$E_2(\frac{3}{2}^+) - E_1(\frac{3}{2}^+)$	467(11)	457(10)	454(12)	458.9(9.9)	454(12)	456(15)	457(12)	456(12)
$E_3(\frac{3}{2}^+) - E_1(\frac{3}{2}^+)$	617(11)	607(10)	571(14)	576(15)	563(14)	568(20)	570(14)	569(14)
$E_4(\frac{3}{2}^+) - E_1(\frac{3}{2}^+)$	661(12)	650(12)	614(15)	622(16)	606(15)	611(21)	614(15)	612(15)
$E_1(\frac{5}{2}^+) - E_1(\frac{3}{2}^+)$	617(11)	606(11)	570(14)	581(14)	570(14)	573(20)	576(14)	573(14)
$E_2(\frac{5}{2}^+) - E_1(\frac{3}{2}^+)$	662(12)	651(12)	610(15)	631(16)	610(15)	613(21)	617(15)	613(15)
$E_1(\frac{7}{2}^+) - E_1(\frac{3}{2}^+)$	617(11)	607(10)	568(13)	591(14)	575(13)	577(19)	580(13)	576(13)
$E_1(\frac{1}{2}^-) - E_1(\frac{3}{2}^+)$	358.6(6.8)	356.1(6.0)	330.3(6.0)	356.0(6.4)	333.7(6.0)	335.1(6.1)	339.3(6.2)	334.5(6.1)
$E_1(\frac{3}{2}^-) - E_1(\frac{3}{2}^+)$	358.6(6.8)	356.1(6.0)	343.3(6.4)	348.9(6.6)	339.4(6.3)	342.0(6.4)	344.5(6.5)	342.7(6.4)
$E_1(\frac{1}{2}^+) - E_1(\frac{7}{2}^+)$	−25.6(1.3)	−24.8(1.2)	−22.6(1.5)	−31.7(1.5)	−29.8(1.8)	−28.7(1.7)	−29.1(1.6)	−27.5(1.6)
$E_2(\frac{1}{2}^+) - E_1(\frac{7}{2}^+)$	−0.023(17)	−0.017(16)	1.4(1.0)	−18.64(99)	−17.2(1.3)	−13.5(1.1)	−13.63(95)	−10.51(98)
$E_3(\frac{3}{2}^+) - E_1(\frac{7}{2}^+)$	−0.023(17)	−0.017(16)	2.21(74)	−15.60(84)	−11.7(1.1)	−8.94(87)	−9.51(77)	−6.67(78)
$E_4(\frac{3}{2}^+) - E_1(\frac{7}{2}^+)$	44.0(1.6)	43.6(1.5)	45.3(2.1)	31.3(1.8)	31.5(1.8)	34.5(2.0)	34.5(2.0)	36.6(2.1)
$E_1(\frac{5}{2}^+) - E_1(\frac{7}{2}^+)$	−0.80(37)	−0.77(35)	1.28(44)	−9.66(54)	−4.94(66)	−3.69(54)	−4.30(48)	−2.59(48)
$E_2(\frac{5}{2}^+) - E_1(\frac{7}{2}^+)$	44.3(1.6)	43.9(1.5)	41.3(1.9)	40.3(2.2)	35.0(1.8)	36.5(1.9)	37.1(2.0)	37.4(1.9)
$E_1(\frac{1}{2}^-) - E_1(\frac{3}{2}^-)$	0	0	−12.97(45)	7.05(23)	−5.70(35)	−6.96(35)	−5.19(28)	−8.14(37)
$E_4(\frac{3}{2}^+) - E_2(\frac{5}{2}^+)$	−0.28(15)	−0.26(14)	4.02(47)	−9.00(51)	−3.50(50)	−2.06(46)	−2.62(39)	−0.78(45)

It is interesting to compare the QCD results obtained here to the potential-model calculation of Ref. [8] (see Fig. 5 therein). The numbers of states in the considered energy region are in agreement, and the energy differences to the ground state predicted by Ref. [8] are found to be within 10% of the QCD results. However, the potentials used in Ref. [8] did not include any spin-orbit or tensor interactions, so the results obtained there have the exact degeneracies $E_2(\frac{1}{2}^+) = E_3(\frac{3}{2}^+) = E_1(\frac{5}{2}^+) = E_1(\frac{7}{2}^+)$, $E_4(\frac{3}{2}^+) = E_2(\frac{5}{2}^+)$, and $E_1(\frac{1}{2}^-) = E_1(\frac{3}{2}^-)$. As can be seen in Fig. 10, the QCD calculation performed here is so precise that the spin-dependent effects that lift these degeneracies are clearly resolved. These effects will be discussed further in Sec. VI.

Reference [8] also calculated the higher-lying bbb spectrum, and these additional states were all found to be separated by energy gaps of order 300 MeV from the states considered here. Along with the plateaus observed in Figs. 6 and 7, the large energy gaps found in Ref. [8] provide further confidence that the contamination from higher states in the fits of Sec. IV is negligible.

Remarkably, the three energy splittings $E_2(\frac{1}{2}^+) - E_1(\frac{3}{2}^+)$, $E_1(\frac{1}{2}^-) - E_1(\frac{3}{2}^+)$, and $E_2(\frac{3}{2}^+) - E_1(\frac{3}{2}^+)$ that were computed in the early bag-model calculation of Ref. [3] also agree with the results obtained here to within 10%. On the other hand, the energy splittings calculated recently using a quark model in Ref. [15] (see Table 19 therein) are in dramatic disagreement with the QCD results obtained here: by about a factor of 2 for the larger splittings and by about a factor of 10 for the smaller splittings.

VI. DEPENDENCE OF THE SPECTRUM ON THE COEFFICIENTS IN THE NRQCD ACTION

In Sec. V, the bbb spectrum was computed with coefficients c_i in the lattice NRQCD action tuned such that the effective field theory reproduces relativistic QCD. Table V and Figs. 9 and 10 give the best possible results obtained here for the bbb energy levels in the real world. However, with lattice NRQCD, one can perform simulations for arbitrary values of the coefficients c_i. The ability to selectively turn on and off the different terms in the NRQCD action and compute the effect on the bbb energy levels can be exploited to gain deeper insight into the interactions between three heavy quarks.

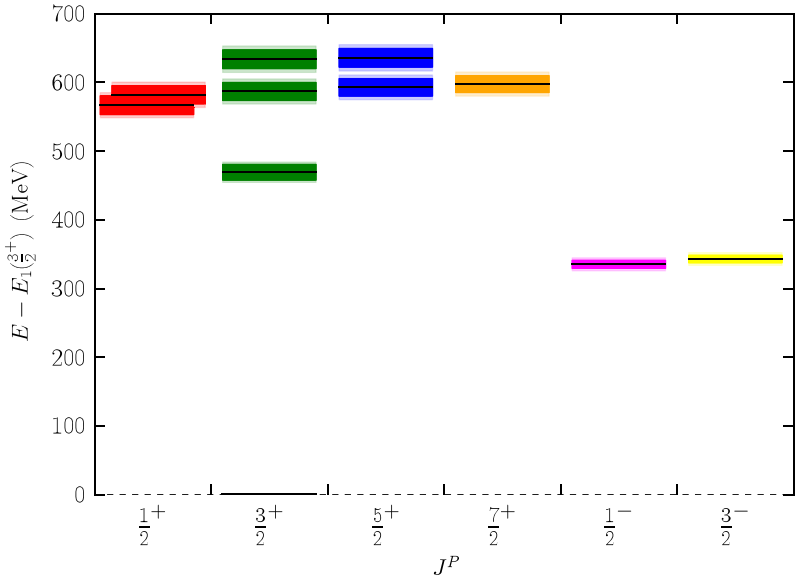

FIG. 9 (color online). Final results for the bbb spectrum relative to the ground state $E_1(\frac{3}{2}^+)$ (see the last column of Table V for the numerical values). The superimposed shaded regions show the statistical/fitting/scale setting uncertainty and the total (including systematic) uncertainty, respectively. The results are highly correlated, and the uncertainties for energy differences between nearby states are in fact much smaller than suggested by this plot. See Fig. 10 for close-ups of the spectra near $E_1(\frac{7}{2}^+)$ and $E_1(\frac{3}{2}^-)$, where advantage is taken of the correlations by computing the energy differences relative to these levels.

The numerical results of this section are summarized in Table VI. Shown there are the values of the bbb energy splittings computed for eight different choices of the coefficients in the NRQCD action. The various terms in the NRQCD action were already discussed in Sec. III, and their coefficients c_i were defined in Eq. (24). The calculations in this section were done for a single gauge-field ensemble only ($a \approx 0.11$ fm, $am_{u,d} = 0.005$), to save computer time. As shown in Sec. V, the dependence of the bbb spectrum on a and $m_{u,d}$ is weak, and therefore a single ensemble is sufficient for the purpose of studying the c_i dependence. In all cases, the b quark mass and the Symanzik-improvement coefficients in the NRQCD action remain unchanged ($am_b = 2.487$, $c_5 = c_6 = 1$). The following discussion focuses on the energy regions near $E_1(\frac{7}{2}^+)$ and $E_1(\frac{3}{2}^-)$, as this is where all the spin-dependent level splittings are found.

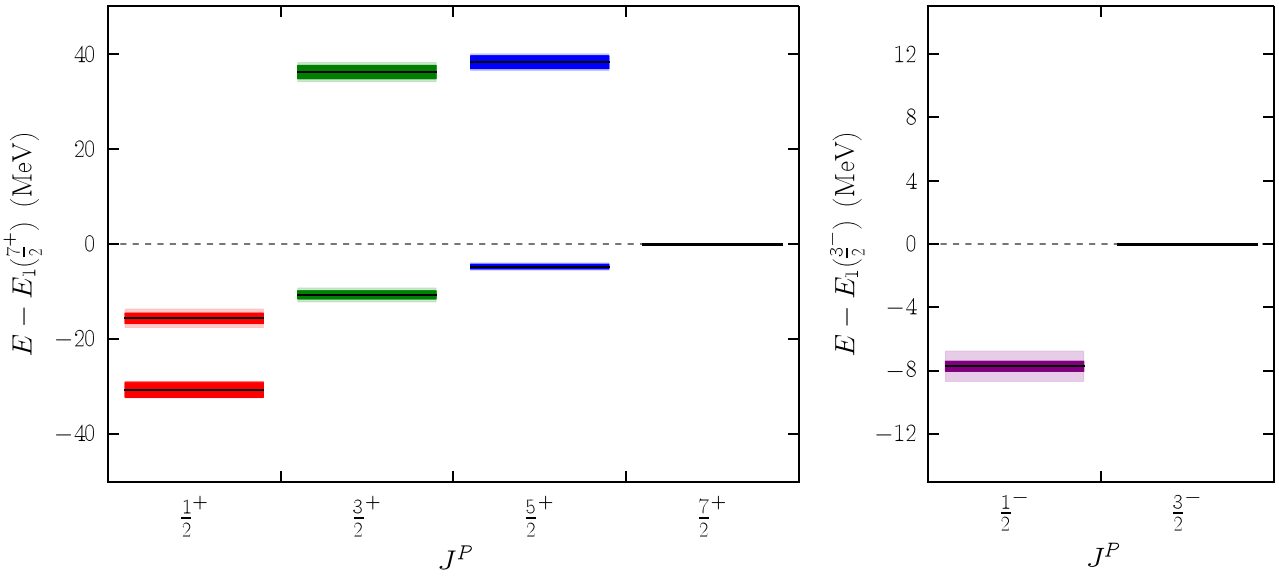

FIG. 10 (color online). Final results for the bbb spectrum relative to $E_1(\frac{7}{2}^+)$ (left panel) and $E_1(\frac{3}{2}^-)$ (right panel), showing only the states in the vicinity of these levels. The superimposed shaded regions show the statistical/fitting/scale setting uncertainty and the total (including systematic) uncertainty, respectively. See the last column of Table V for the numerical values.

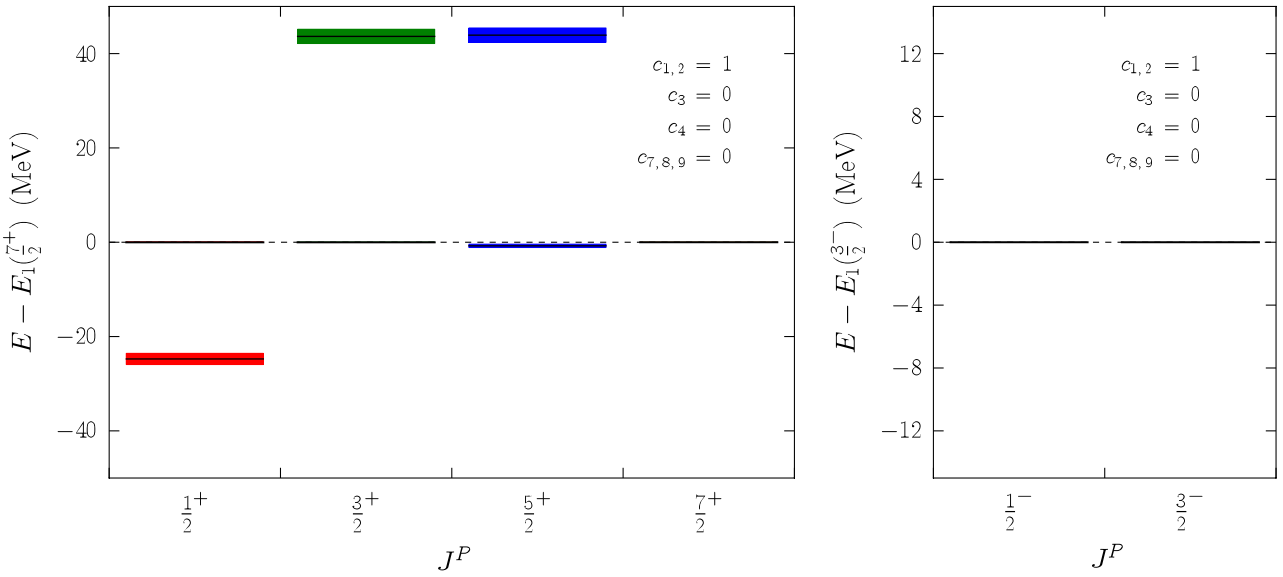

FIG. 11 (color online). Dependence of the spectrum near $E_1(\frac{7}{2}^+)$ and $E_1(\frac{3}{2}^-)$ on the coefficients c_i in the NRQCD action (at $a \approx 0.11$ fm, $am_{u,d} = 0.005$). Shown here is the case of the spin-independent order-v^4 NRQCD action, obtained by setting $c_3 = c_4 = c_7 = c_8 = c_9 = 0$. In the absence of rotational symmetry breaking, this leads to the exact degeneracies $E_2(\frac{1}{2}^+) = E_3(\frac{3}{2}^+) = E_1(\frac{5}{2}^+) = E_1(\frac{7}{2}^+)$, $E_4(\frac{3}{2}^+) = E_2(\frac{5}{2}^+)$, and $E_1(\frac{1}{2}^-) = E_1(\frac{3}{2}^-)$. On the lattice, the relations $E_1(\frac{1}{2}^-) = E_1(\frac{3}{2}^-)$ and $E_2(\frac{1}{2}^+) = E_3(\frac{3}{2}^+)$ are still exact, but the degeneracies with $J > \frac{3}{2}$ levels are only approximate.

The energy splittings in the first column of Table VI were computed with the order-v^2 NRQCD action, which contains only $H_0 = -\frac{1}{2m_b}\Delta^{(2)}$ (and the associated lattice discretization improvement terms with c_5 and c_6). Turning on also the spin-independent order-v^4 terms, $-c_1\frac{1}{8m_b^3} \times (\Delta^{(2)})^2$ and $c_2\frac{ig}{8m_b^2}(\boldsymbol{\nabla}\cdot\tilde{\boldsymbol{E}} - \tilde{\boldsymbol{E}}\cdot\boldsymbol{\nabla})$, gives the results in the second column of Table VI. These results are plotted in Fig. 11. In both cases, the action does not depend on the heavy-quark spin, so L and S become separately conserved quantum numbers, up to the small effects of rotational symmetry breaking introduced by the lattice. In the absence of rotational symmetry breaking, one would then have the exact level degeneracies $E_2(\frac{1}{2}^+) = E_3(\frac{3}{2}^+) = E_1(\frac{5}{2}^+) = E_1(\frac{7}{2}^+)$, $E_4(\frac{3}{2}^+) = E_2(\frac{5}{2}^+)$, and $E_1(\frac{1}{2}^-) = E_1(\frac{3}{2}^-)$. The relations $E_1(\frac{1}{2}^-) = E_1(\frac{3}{2}^-)$ and $E_2(\frac{1}{2}^+) = E_3(\frac{3}{2}^+)$

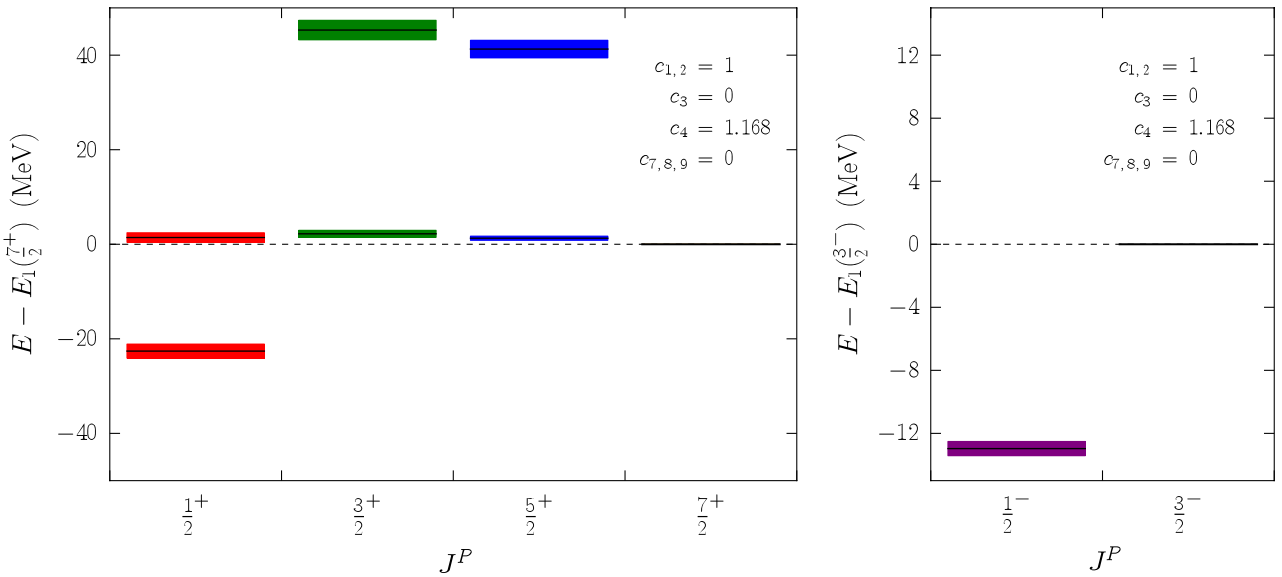

FIG. 12 (color online). Dependence of the spectrum near $E_1(\frac{7}{2}^+)$ and $E_1(\frac{3}{2}^-)$ on the coefficients c_i in the NRQCD action (at $a \approx 0.11$ fm, $am_{u,d} = 0.005$). Shown here is the case of the order-v^4 NRQCD action, but with the coefficient of the operator $\boldsymbol{\sigma}\cdot(\tilde{\boldsymbol{\nabla}} \times \tilde{\boldsymbol{E}} - \tilde{\boldsymbol{E}} \times \tilde{\boldsymbol{\nabla}})$ set to zero, so that the only remaining spin-dependent interaction is $-c_4\frac{g}{2m_b}\boldsymbol{\sigma}\cdot\tilde{\boldsymbol{B}}$.

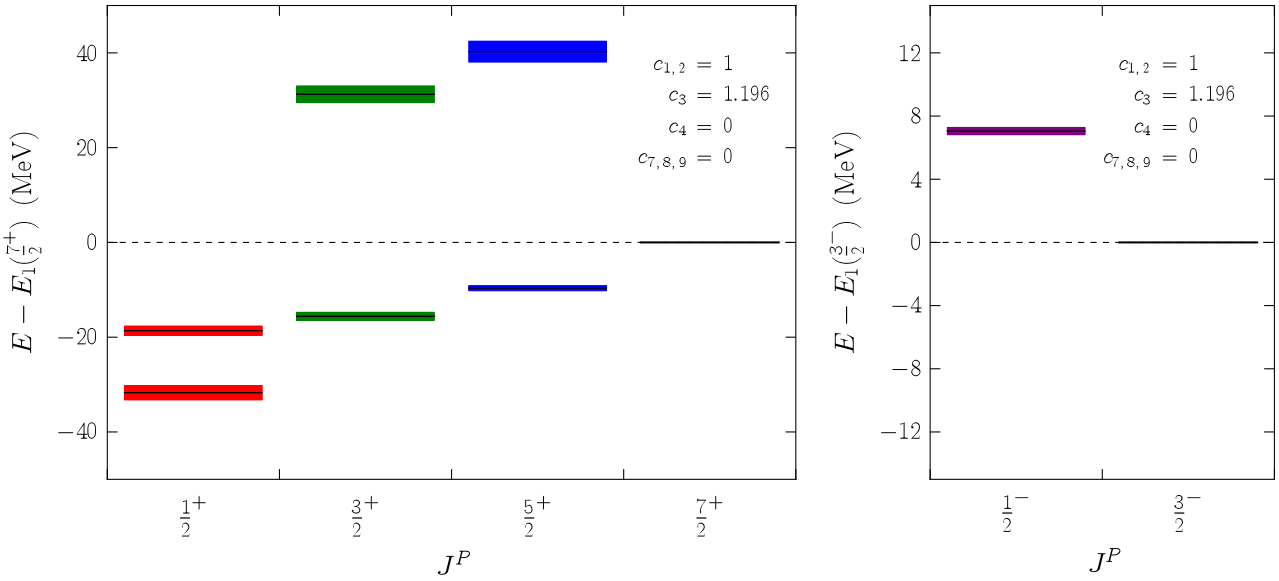

FIG. 13 (color online). Dependence of the spectrum near $E_1(\frac{7}{2}^+)$ and $E_1(\frac{3}{2}^-)$ on the coefficients c_i in the NRQCD action (at $a \approx 0.11$ fm, $am_{u,d} = 0.005$). Shown here is the case of the order-v^4 NRQCD action, but with the coefficient of the operator $\boldsymbol{\sigma} \cdot \tilde{\boldsymbol{B}}$ set to zero, so that the only remaining spin-dependent interaction is $-c_3 \frac{g}{8m_b^2} \boldsymbol{\sigma} \cdot (\tilde{\boldsymbol{\nabla}} \times \tilde{\boldsymbol{E}} - \tilde{\boldsymbol{E}} \times \tilde{\boldsymbol{\nabla}})$.

actually remain exact on the lattice, an observation that can be related to the trivial subduction of these two J values into lattice irreps (cf. Sec. II B). The degeneracies with $J > \frac{3}{2}$ are only approximate, but the splittings remain very small. Note that the energies quoted here for the higher-J levels were obtained by averaging over the different irreps into which a continuum level splits [see the discussion around Eq. (33); also see Table IV for the size of the original splittings between the different irreps].

Next, Fig. 12 shows the spectrum after additionally turning on the leading interaction with the chromomagnetic moment of the heavy quark:

$$-c_4 \frac{g}{2m_b} \boldsymbol{\sigma} \cdot \tilde{\boldsymbol{B}}. \tag{37}$$

This interaction causes small positive splittings $[E_2(\frac{1}{2}^+) - E_1(\frac{7}{2}^+)]_{\text{subtr}} = 1.5(1.0)$ MeV, $[E_3(\frac{3}{2}^+) - E_1(\frac{7}{2}^+)]_{\text{subtr}} = 2.23(74)$ MeV, $[E_1(\frac{5}{2}^+) - E_1(\frac{7}{2}^+)]_{\text{subtr}} = 2.05(56)$ MeV, and $[E_4(\frac{3}{2}^+) - E_2(\frac{5}{2}^+)]_{\text{subtr}} = 4.28(49)$ MeV, where the

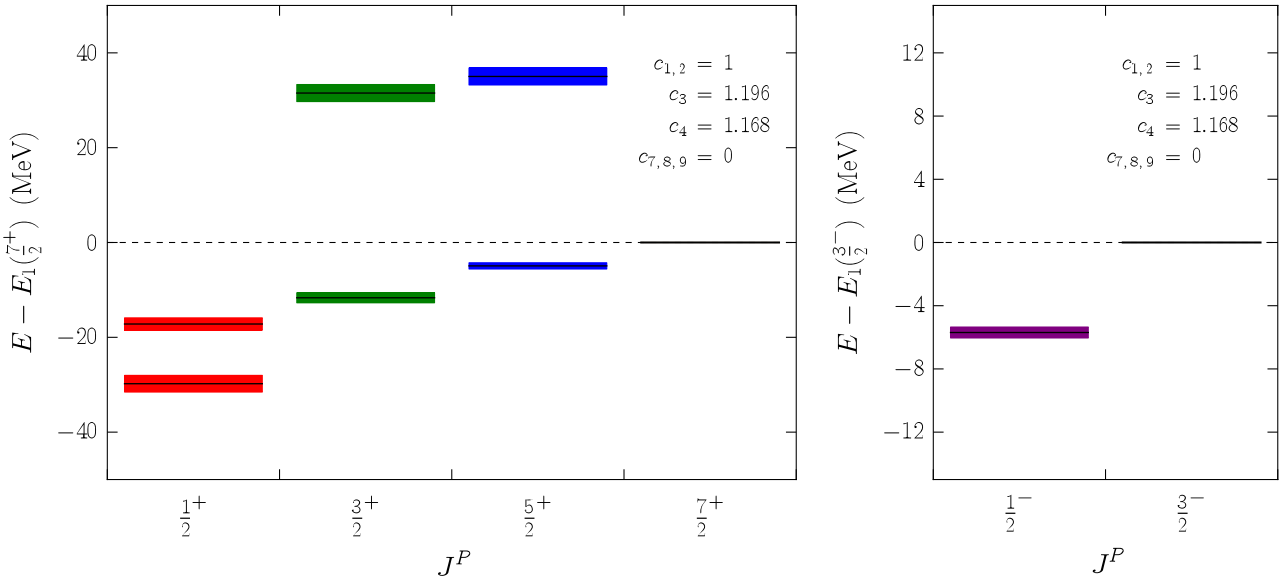

FIG. 14 (color online). Dependence of the spectrum near $E_1(\frac{7}{2}^+)$ and $E_1(\frac{3}{2}^-)$ on the coefficients c_i in the NRQCD action (at $a \approx 0.11$ fm, $am_{u,d} = 0.005$). Shown here is the case of the complete order-v^4 NRQCD action.

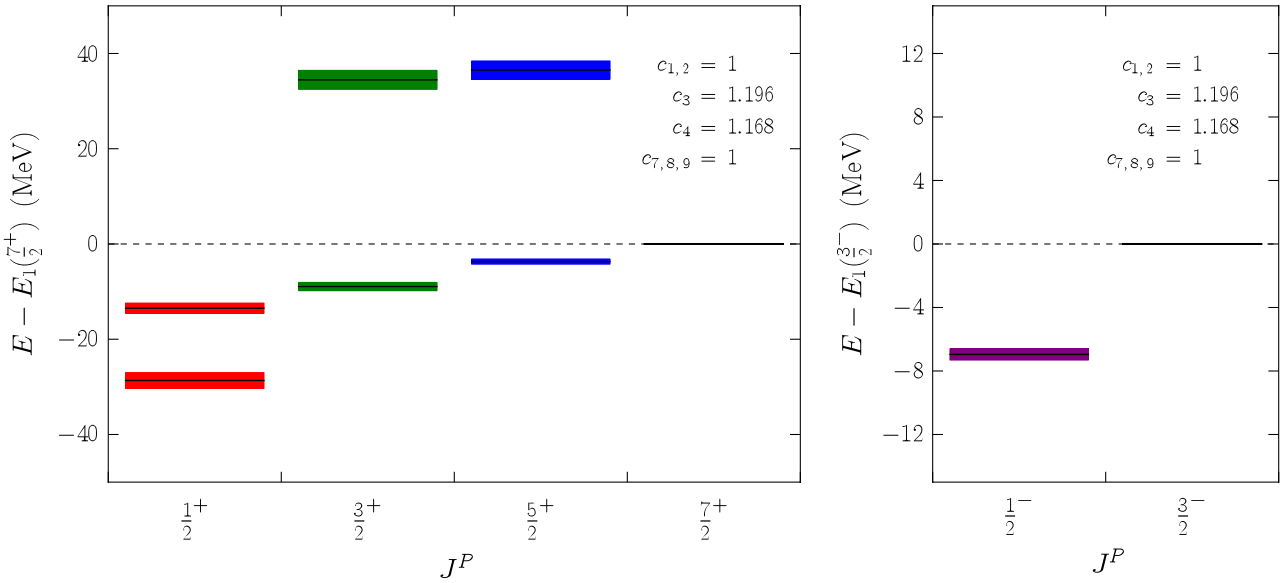

FIG. 15 (color online). Dependence of the spectrum near $E_1(\frac{7}{2}^+)$ and $E_1(\frac{3}{2}^-)$ on the coefficients c_i in the NRQCD action (at $a \approx 0.11$ fm, $am_{u,d} = 0.005$). Shown here is the case of the complete NRQCD action as used in the main calculations of this work, including all terms of order v^4 as well as the spin-dependent order-v^6 terms.

rotational-symmetry-breaking-induced splittings seen at $c_4 = 0$ (second column of Table VI) have been subtracted. The operator (37) also introduces a very significant splitting of the two odd-parity levels considered here: $E_1(\frac{1}{2}^-) - E_1(\frac{3}{2}^-) = -12.97(45)$ MeV. For heavy quarkonium, the operator (37) is mainly associated with spin-spin and tensor interactions. However, simple potential models for baryons that include only spin-spin and tensor interactions predict $E_1(\frac{1}{2}^-) - E_1(\frac{3}{2}^-) = 0$ [51–53]. Thus, one can conclude that the operator (37) also plays an important role in the generation of spin-orbit interactions. This can indeed be seen in the derivation of spin-dependent potentials using pNRQCD [54].

The other spin-dependent interaction of order v^4 is given by

$$-c_3 \frac{g}{8m_b^2} \boldsymbol{\sigma} \cdot (\tilde{\boldsymbol{\nabla}} \times \tilde{\boldsymbol{E}} - \tilde{\boldsymbol{E}} \times \tilde{\boldsymbol{\nabla}}). \tag{38}$$

Setting $c_4 = 0$ again, and turning on the interaction (38) instead, produces the results shown in Fig. 13. For the bbb levels considered here, the operator (38) results in spin splittings with the opposite sign compared to those introduced by (37): $[E_2(\frac{1}{2}^+) - E_1(\frac{7}{2}^+)]_{\text{subtr}} = -18.63(99)$ MeV, $[E_3(\frac{3}{2}^+) - E_1(\frac{7}{2}^+)]_{\text{subtr}} = -15.58(84)$ MeV, $[E_1(\frac{5}{2}^+) - E_1(\frac{7}{2}^+)]_{\text{subtr}} = -8.89(64)$ MeV, $E_4[(\frac{3}{2}^+) - E_2(\frac{5}{2}^+)]_{\text{subtr}} = -8.74(53)$ MeV, and $E_1(\frac{1}{2}^-) - E_1(\frac{3}{2}^-) = 7.05(23)$ MeV. Notice, in particular, that for the bbb levels with approximate structure $L = 2$, $S = \frac{3}{2}$, the effect of (38) is an order of magnitude larger than the effect of (37). Furthermore, the shifts introduced for these levels by the operator (38) are approximately proportional to $2\boldsymbol{L} \cdot \boldsymbol{S} = J(J+1) - L(L+1) - S(S+1)$. This is what is expected for a spin-orbit interaction in baryon levels with totally symmetric spatial wave functions [55].

Next, Fig. 14 shows the bbb spectrum with both (37) and (38) turned on (fifth column of Table VI). For $[E_2(\frac{1}{2}^+) - E_1(\frac{7}{2}^+)]_{\text{subtr}}$ and $E_1(\frac{1}{2}^-) - E_1(\frac{3}{2}^-)$, the new results are consistent with the sums of the results from separately turning on (37) and (38), but there is some evidence for nonlinear behavior in the other spin splittings. For example, the splitting $[E_1(\frac{5}{2}^+) - E_1(\frac{7}{2}^+)]_{\text{subtr}}$ is equal to $-4.17(74)$ MeV now, while the sum of the splittings obtained from separately activating (37) and (38) is $-6.85(85)$ MeV. Of course there is no reason to expect linearity here: the lattice calculation is fully nonperturbative.

Having included both (37) and (38), the action is now complete through order v^4. As can be seen by comparing the results in the first and the fifth columns of Table VI, the radial and orbital bbb energy splittings obtained with the order-v^2 and order-v^4 NRQCD actions differ by $\lesssim 10\%$, demonstrating the convergence of the NRQCD expansion with $v^2 \approx 0.1$ as in bottomonium. Finally, turning on additionally the spin-dependent order-v^6 terms by setting $c_7 = c_8 = c_9 = 1$ gives the results in the sixth column of Table VI, which are plotted in Fig. 15. The order-v^6 terms affect some of the bbb spin splittings by as much as 30%, showing that including these terms is essential to obtain precise results. Most of the bbb spin splittings considered here decrease in magnitude when the order-v^6 terms are included in the NRQCD action, as is familiar from bottomonium [36]. However, one notable exception to this rule is found here: the order-v^6 corrections *increase* the magnitude of $E_1(\frac{1}{2}^-) - E_1(\frac{3}{2}^-)$.

VII. CONCLUSIONS

In this work, the first nonperturbative QCD calculation of the baryonic analogue of the bottomonium spectrum was performed. By combining improved lattice NRQCD [35] with other powerful techniques that have been developed more recently, the energies of ten bbb excited states were computed with high precision. The calculations include $2+1$ dynamical flavors of light quarks, and the bbb spectrum was extrapolated to the physical pion mass. The main results are given in Table V and are plotted in Figs. 9 and 10.

The reliable identification of triply bottom baryon states with angular momentum up to $J = \frac{7}{2}$ was greatly simplified by using interpolating operators constructed with the subduction method of Ref. [33]. As already observed in Ref. [33] for light baryons, the cross correlations between interpolating operators subduced from different values of J are small. In the present work, it was additionally shown that these overlaps decrease when the lattice spacing is reduced. Furthermore, it was possible to resolve the small energy splittings of continuum bbb levels with $J > \frac{3}{2}$ into the different irreducible representations of the double-cover octahedral group. It was shown that these splittings also decrease when the lattice spacing is reduced (see Table IV), providing another demonstration of rotational symmetry restoration. While the suppression of mixing between different J values is a general consequence of the approximate rotational symmetry, additional suppressions were observed here for the triply heavy baryon two-point functions between operators constructed using different values of L or S. This feature is likely to be a consequence of the large b quark mass, resulting in a suppression of the spin-orbit coupling and hence an approximate individual conservation of L and S (the total orbital angular momentum and total quark spin).

To implement the b quarks on the lattice, a NRQCD action including the spin-dependent order-v^6 terms was used here, and the coefficients of the spin-dependent order-v^4 terms were tuned nonperturbatively. Together with the high statistics, this allowed the calculation of the bbb spin splittings with $\sim$1 MeV total uncertainty. To learn more about the forces between three heavy quarks, additional simulations were performed on one ensemble for several "unphysical" choices of coefficients in the NRQCD action, thereby disentangling the contributions of different NRQCD operators to the bbb energy splittings. These additional simulations also clearly demonstrated the convergence of the velocity expansion for bbb baryons and facilitated the estimates of the systematic uncertainties given in Table V.

The lattice QCD results obtained here for the triply bottom baryon spectrum provide a unique opportunity to test quark models for baryons in the regime where the description using potentials is expected to work best. Most of the past potential-model calculations of baryon excited states have focused on *light* baryons, for which some experimental data are available. However, quark-model descriptions are bound to remain poor approximations for these complicated systems. Now that precise lattice QCD results for the much cleaner bbb spectrum are available for comparison, it is desirable to perform new continuum-based calculations for triply heavy baryons, using, for example, the quark model of Ref. [56], or the modern pNRQCD approach [21,57].

ACKNOWLEDGMENTS

I thank William Detmold, Robert Edwards, and Kostas Orginos for useful discussions, and the RBC/UKQCD Collaboration for making their gauge-field ensembles available. This work was supported by the U.S. Department of Energy under Grant No. DE-SC0001784. The computations were performed using resources at the National Energy Research Scientific Computing Center and the National Institute for Computational Sciences (XSEDE Grant No. TG-PHY080014N).

[1] N. Brambilla *et al.*, Eur. Phys. J. C **71**, 1534 (2011).
[2] W. Ponce, Phys. Rev. D **19**, 2197 (1979).
[3] P. Hasenfratz, R. R. Horgan, J. Kuti, and J. M. Richard, Phys. Lett. **94B**, 401 (1980).
[4] J. D. Bjorken, Report No. FERMILAB-Conf-85/69, 1985.
[5] M. Tsuge, T. Morii, and J. Morishita, Mod. Phys. Lett. A **1**, 131 (1986); **2**, 283(E) (1987).
[6] J. L. Basdevant and S. Boukraa, Z. Phys. C **30**, 103 (1986).
[7] A. Martin and J. M. Richard, Phys. Lett. B **355**, 345 (1995).
[8] B. Silvestre-Brac, Few-Body Syst. **20**, 1 (1996).
[9] J. Schaffner-Bielich and A. P. Vischer, Phys. Rev. D **57**, 4142 (1998).
[10] J. Vijande, H. Garcilazo, A. Valcarce, and F. Fernandez, Phys. Rev. D **70**, 054022 (2004).
[11] S. Migura, D. Merten, B. Metsch, and H. R. Petry, Eur. Phys. J. A **28**, 41 (2006).
[12] A. Faessler *et al.*, Phys. Rev. D **73**, 094013 (2006).
[13] A. P. Martynenko, Phys. Lett. B **663**, 317 (2008).
[14] S. M. Gerasyuta and E. E. Matskevich, Int. J. Mod. Phys. E **17**, 585 (2008).
[15] W. Roberts and M. Pervin, Int. J. Mod. Phys. A **23**, 2817 (2008).
[16] A. Bernotas and V. Simonis, Lith. J. Phys. **49**, 19 (2009).
[17] J. M. Flynn, E. Hernandez, and J. Nieves, Phys. Rev. D **85**, 014012 (2012).

[18] J. R. Zhang and M. Q. Huang, Phys. Lett. B **674**, 28 (2009).
[19] Z.-G. Wang, arXiv:1112.2274.
[20] Y. Jia, J. High Energy Phys. 10 (2006) 073.
[21] F. J. Llanes-Estrada, O. I. Pavlova, and R. Williams, arXiv:1111.7087.
[22] N. Brambilla, J. Ghiglieri, and A. Vairo, Phys. Rev. D **81**, 054031 (2010).
[23] Y.-Q. Chen and S.-Z. Wu, J. High Energy Phys. 08 (2011) 144; 09 (2011) 089(E).
[24] S. Meinel, Phys. Rev. D **82**, 114514 (2010).
[25] W. Melnitchouk *et al.*, Phys. Rev. D **67**, 114506 (2003).
[26] N. Mathur *et al.*, Phys. Lett. B **605**, 137 (2005).
[27] D. Guadagnoli, M. Papinutto, and S. Simula, Phys. Lett. B **604**, 74 (2004).
[28] T. Burch *et al.*, Phys. Rev. D **74**, 014504 (2006).
[29] S. Basak *et al.*, Phys. Rev. D **76**, 074504 (2007).
[30] J. M. Bulava *et al.*, Phys. Rev. D **79**, 034505 (2009).
[31] J. Bulava *et al.*, Phys. Rev. D **82**, 014507 (2010).
[32] M. S. Mahbub *et al.* (CSSM Lattice Collaboration), Phys. Lett. B **707**, 389 (2012).
[33] R. G. Edwards, J. J. Dudek, D. G. Richards, and S. J. Wallace, Phys. Rev. D **84**, 074508 (2011).
[34] B. A. Thacker and G. P. Lepage, Phys. Rev. D **43**, 196 (1991).
[35] G. P. Lepage, L. Magnea, C. Nakhleh, U. Magnea, and K. Hornbostel, Phys. Rev. D **46**, 4052 (1992).
[36] S. Meinel, Phys. Rev. D **82**, 114502 (2010).
[37] Y. Aoki *et al.* (RBC and UKQCD Collaborations), Phys. Rev. D **83**, 074508 (2011).
[38] D. B. Kaplan, Phys. Lett. B **288**, 342 (1992).
[39] Y. Shamir, Nucl. Phys. **B406**, 90 (1993).
[40] V. Furman and Y. Shamir, Nucl. Phys. **B439**, 54 (1995).
[41] R. C. Johnson, Phys. Lett. **114B**, 147 (1982).
[42] M. Peardon *et al.* (Hadron Spectrum Collaboration), Phys. Rev. D **80**, 054506 (2009).
[43] A. C. Lichtl, Ph.D. thesis, Carnegie Mellon University [arXiv:hep-lat/0609019].
[44] C. Morningstar and M. J. Peardon, Phys. Rev. D **69**, 054501 (2004).
[45] Y. Iwasaki, Report No. UTHEP-118, 1983.
[46] Y. Iwasaki and T. Yoshie, Phys. Lett. **143B**, 449 (1984).
[47] D. J. Antonio *et al.* (RBC/UKQCD Collaboration), Phys. Rev. D **75**, 114501 (2007).
[48] G. P. Lepage and P. B. Mackenzie, Phys. Rev. D **48**, 2250 (1993).
[49] A. Gray *et al.*, Phys. Rev. D **72**, 094507 (2005).
[50] K. Nakamura *et al.* (Particle Data Group Collaboration), J. Phys. G **37**, 075021 (2010).
[51] N. Isgur and G. Karl, Phys. Rev. D **18**, 4187 (1978).
[52] K.-T. Chao, N. Isgur, and G. Karl, Phys. Rev. D **23**, 155 (1981).
[53] D. Gromes, Z. Phys. C **18**, 249 (1983).
[54] A. Pineda and A. Vairo, Phys. Rev. D **63**, 054007 (2001); **64**, 039902(E) (2001).
[55] D. Gromes and I. O. Stamatescu, Nucl. Phys. **B112**, 213 (1976).
[56] S. Capstick and N. Isgur, Phys. Rev. D **34**, 2809 (1986).
[57] N. Brambilla, A. Vairo, and T. Rosch, Phys. Rev. D **72**, 034021 (2005).